J. Fluid Mech. (2024), *vol*. 987, A13, doi:10.1017/jfm.2024.299

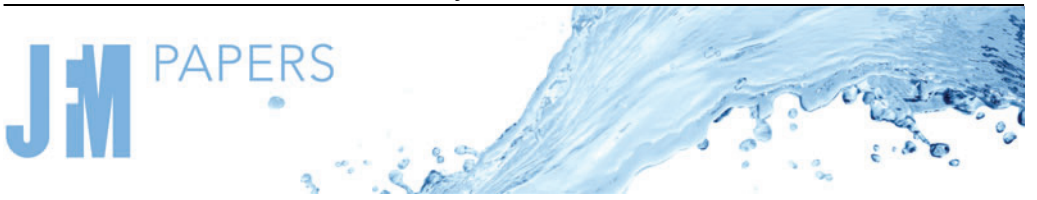

Boundary-layer instability on a highly swept fin on a cone at Mach 6

Madeline M. Peck[1],†, **Koen J. Groot**[1] **and Helen L. Reed**[1]

[1]Department of Aerospace Engineering, Texas A&M University, College Station, TX 77843, USA

(Received 30 September 2023; revised 4 February 2024; accepted 21 March 2024)

The growth and characteristics of linear, oblique instabilities on a highly swept fin on a straight cone in Mach 6 flow are examined. Large streamwise pressure gradients cause doubly inflected cross-flow profiles and reversed flow near the wall, which necessitates using the harmonic linearized Navier–Stokes equations. The cross-flow instability is responsible for the most-amplified disturbances, however, not all disturbances show typical cross-flow characteristics. Distinct differences in perturbation structure are shown between small (∼3–5 mm) and large (∼10 mm) wavelength disturbances at the unit Reynolds number $Re' = 11 \times 10^6$ m^{-1}. As a result, amplification measurements based solely on wall quantities bias a most-amplified disturbance assessment towards larger wavelengths and lower frequencies than would otherwise be determined by an off-wall total-energy approach. A spatial-amplification energy-budget analysis demonstrates (i) that wall-normal Reynolds-flux terms dictate the local growth rate, despite other terms having a locally larger magnitude and (ii) that the Reynolds-stress terms are responsible for large-wavelength disturbances propagating closer to the wall compared with small-wavelength disturbances. Additionally, the effect of free-stream unit Reynolds number and small yaw angles on the perturbation amplification and energy budget is considered. At a higher Reynolds number ($Re' = 22 \times 10^6$ m^{-1}), the most-amplified wavelength shrinks. Perturbations do not behave self-similarly in the thinner boundary layer, and the shift in most-amplified wavelength is due to decreased dissipation relative to the lower-Reynolds-number case. Small yaw angles produce a streamwise shift in the boundary layer and disturbance amplification. The yaw results quantify a potential uncertainty source in experiments and flight.

Key words: boundary layer stability, hypersonic flow, compressible boundary layers

† Email address for correspondence: mad_mcmillan@tamu.edu

1. Introduction

Hypersonic flow over a swept control surface can experience a large cross-flow velocity component in the boundary layer and therefore be susceptible to the cross-flow instability. This can lead to transition from a laminar to a turbulent boundary layer. Understanding and modelling the physical mechanisms leading to this transition is desirable for multiple reasons. The results lead to smaller, more manageable uncertainties in flow properties, and advances in technologies for assessment, design and control. Regarding control, delaying transition can reduce the total heat flux and drag on the surface, while promoting turbulence may prevent boundary-layer separation on movable control surfaces. Any attempt at flow control depends on understanding the relevant instability mechanisms and what affects them, and is generally most efficient when one capitalizes on the most unstable disturbances present. However, making meaningful predictions on instability characteristics in complex flows and further untangling the driving mechanisms become both more important and more challenging.

Often, flow over realistic vehicles features large velocity components in three dimensions. In these flows, throughout the incompressible to hypersonic speed regimes, the cross-flow instability can play an important role in the transition process. The cross-flow instability is caused by the generalized inflection point formed by the cross-flow velocity component (Saric, Reed & White 2003). Typically, researchers distinguish between stationary (zero frequency) and travelling cross-flow disturbances, as each type is receptive to different external triggers such as surface roughness and free-stream noise, respectively (Bippes 1999). Consequently, stationary and travelling waves are expected to dominate in quiet and noisy flows, respectively, although both waves can coexist (e.g. Borg, Kimmel & Stanfield 2015; Craig & Saric 2016). A possible path to transition is as follows: external disturbances induce perturbations in the flow through the receptivity process, which then can grow exponentially (prior to nonlinear interactions) if the initial perturbation amplitude is small enough. In flight environments, stationary cross-flow disturbances grow until a large, stationary vortex develops and nonlinear effects cause the vortex to saturate (e.g. Haynes & Reed 2000). Multiple types of high-frequency secondary instabilities with large growth rates can develop in the highly inflectional modified base flow and will eventually cause the flow to break down to turbulence (Kohama, Saric & Hoos 1991; Malik, Li & Chang 1994; Koch *et al.* 2000; White & Saric 2005). Recent studies on hypersonic cross-flow instability (Craig & Saric 2016; Moyes *et al.* 2017; Xu *et al.* 2019) demonstrate the many similarities between low- and high-speed cases, and indicate that the lessons learned at low speeds can help inform current hypersonic cross-flow research.

In recent hypersonic boundary-layer-stability test campaigns on complex geometries, experiments and computations demonstrate that multiple instability mechanisms can be active at once. Often, researchers attempt to divide the flow into certain regions where possible instability mechanisms can be narrowed down to one or two likely candidates. For example, the HIFiRE-5 tests on an elliptic cone show attachment line instabilities, second (or 'Mack') modes, and shear-layer modes in addition to the stationary and travelling cross-flow modes (Borg *et al.* 2015; Juliano, Borg & Schneider 2015; Paredes *et al.* 2016). The shear modes are generally confined to the mushroom structure along the semi-minor axis, Mack-mode instabilities are found along the semi-major axis and cross-flow modes and oblique Mack modes are found between these regions. Similar instabilities are relevant on the HyTRV vehicle, and segments of the geometry are studied separately to try and isolate the dominant instabilities (Chen *et al.* 2022*a*). In some low-speed cases, such as on a natural-laminar-flow airfoil or similar modelled cases, regions of favourable and

adverse pressure gradients can support both the cross-flow and first-mode instabilities (e.g. Wassermann & Kloker 2005). The dominance of one instability over another during transition in this case requires an analysis that considers nonlinear effects, however, the possible nonlinear scenarios chosen for examination can be guided by linear stability theory, where characteristics of the underlying laminar base flow can provide a first guess on possible instabilities and their regions of influence. Therefore, it is useful to understand what general characteristics of the flow result in specific instabilities.

Unfortunately, identifying instability mechanisms that neatly align with canonical examples is becoming more difficult. Several studies demonstrate how the influence of Mach number exacerbates this issue. For example, Liu (2022) showed that the unstable frequency and wavenumber regions representing the cross-flow and first-mode instabilities in Falkner–Skan–Cooke flow are distinct at incompressible speeds, but can no longer be distinguished at Mach 4.5. Similarly, Özgen & Kırcalı (2008) calculate neutral stability curves for flat-plate boundary layers up to Mach 10, and show how the unstable regions belonging to the first and second modes merge into one indistinguishable neutral curve at Mach 10. In more complex boundary layers, such as flow modified by a saturated stationary cross-flow vortex, it can be difficult to distinguish between proper secondary instabilities and modulated travelling cross-flow or Mack modes (e.g. Li *et al.* 2016; Moyes *et al.* 2017; Edelman & Schneider 2018). In these cases, rather than attempting to classify instabilities as a well-known type, one way to better understand possible transition scenarios is to identify key mechanisms driving the growth. This provides critical insight into why particular disturbances become most amplified. In non-self-similar boundary layers, dominant mechanisms can be complicated by changes in the streamwise or spanwise directions. For example, research on cross-flow over a forward-facing step identified novel mechanisms that impact the instability growth rates on a local scale (Eppink 2020; Rius-Vidales & Kotsonis 2021). In shock–boundary-layer interactions (SBLIs), Niessen *et al.* (2023) used an energy analysis to show how the large streamwise gradients resulting from the SBLI can result in significant stabilizing or destabilizing effects, depending on the disturbance location relative to the SBLI. These studies illustrate how in-depth analysis of physical mechanisms provide important insight when studying instabilities in complex flows.

One flow that has drawn recent interest in the hypersonic community is flow over a slender, straight cone with a single, highly swept fin (usually swept between 70 and 75°), where the fin is intended to model a hypersonic control surface. Initial direct numerical simulations of Mach 6 flow over this geometry revealed two large, stationary vortices, one each on the cone and fin surface, and an unusually large cross-flow velocity near the fin leading edge (Knutson, Gs & Candler 2018). The researchers suggest that the cross-flow instability may be dominant on the fin due to the high cross-flow velocity, but this was not further investigated. Multiple wind-tunnel experiments followed which focused on the cone vortex, which is the first feature to exhibit transition (see Turbeville 2021). A few experiments in this campaign examined the fin, but did not observe evidence of transition (near the leading edge or otherwise). Accompanying computations using the linear parabolized stability equations (LPSE) indicated that, in the Reynolds-number range examined, the cross-flow instability on the fin was insignificant compared with the second mode (Mullen *et al.* 2019). A second set of experiments, conducted in the Air Force's Mach 6 Ludwieg Tube, focused on identifying transition near the leading edge (Middlebrooks *et al.* 2022). Using surface heat-flux measurements, heat-flux striations and a transition front were identified at the highest unit Reynolds number tested ($Re' = 22 \times 10^6$ m^{-1}). The striations were approximately aligned with the free-stream direction, and wavelet

analysis revealed a characteristic wavelength of approximately 10 mm near the transition front.

The flow between the transition front and the fin leading edge is subject to very large cross-flow velocities, strong pressure gradients perpendicular to the leading edge and, at the end of the domain examined, a large stationary vortex. These factors result in a complex flow where the instability mechanisms are not immediately clear. In order to understand how disturbances evolve in the complex flow on the fin, we will use the harmonic linearized Navier–Stokes (HLNS) equations to model disturbances. Section 2 will describe the methods used to generate the base flow and set up the HLNS problem. The disturbances will be characterized and the dominant wavelengths and frequencies identified in § 3. A spatial-growth energy-budget analysis will be formulated in § 4 to provide insight into perturbation-energy mechanisms, and dominant contributors to energy production and destruction will be identified. Finally, the effect of Reynolds number (§ 5) and small yaw angles (§ 6) will be explored to provide insight into a few of the parameters governing the flow. Section 7 summarizes important results.

2. Methods

The growth of linear perturbations on the fin are modelled using the linearized Navier–Stokes equations formulated for a calorically perfect gas. Perturbations of interest (q') are assumed to be small (of $O(\epsilon)$), therefore the instantaneous flow (Q) can be described as

$$Q(x^i, t) = \overline{Q}(x^i) + \epsilon q'(x^i, t). \tag{2.1}$$

Terms which consist solely of steady-state base-flow variables ($\overline{Q}$) automatically satisfy the steady Navier–Stokes equations and are eliminated from the system. For a linear analysis, it is assumed that $\mathcal{O}(\epsilon^2)$ and higher-order terms are small and can be neglected. To solve the resulting linear system of equations for the unknown perturbation variables, a steady-state, laminar base flow is first generated, then the stability equations are solved. The methods used to generate the steady-state base flows are reviewed first, followed by the linear stability methods.

2.1. *Geometry and laminar base flow*

The geometry used in this work is based off of the model used in experiments by Middlebrooks *et al.* (2022). The body is a straight cone with a half-angle of 7° and a circular nose tip with a radius of 5.323 mm. Starting at $X = 0.127$ m (measured axially from the fictional sharp nose tip), there is a single fin swept at 70° with respect to the vertical Y axis (see figure 1). The leading edge of the fin is circular with a radius of 3.175 mm measured in the direction perpendicular to the leading edge. Due to experimental requirements concerning the structural integrity of the wind-tunnel model, the fin thickness increases beginning at 32 mm from the leading edge of the fin, measured perpendicular to the leading edge. The thickness changes from 6.35 to 9.525 mm. Additionally, beginning at $X = 0.391$ m, the fin is truncated to be a constant 63.5 mm above the cone surface. This truncation leads to a sharp corner on the wind-tunnel model, which is modified in the computational model with a fillet to add a rounded edge with the same radius as the leading edge. This is done to improve the computational grid. For more details on the wind-tunnel model, see Middlebrooks *et al.* (2021).

Free-stream conditions are derived from the wind-tunnel conditions for the experiments run in the Air Force Academy's Mach 6 Ludwieg Tube. Two unit Reynolds numbers are

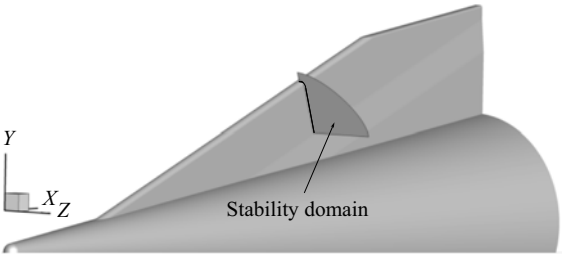

Figure 1. Fin-cone geometry and global coordinate system. Here, X, Y and Z are global coordinates measured from the fictional sharp tip of the cone at the symmetry plane. The stability domain is included to demonstrate its leading-edge-orthogonal orientation.

Re' [m^{-1}]	ρ_∞ [kg m^{-3}]	T_∞ [K]	M_∞	T_{wall} [K]
11×10^6	0.0462	58.59	6.0	300
22×10^6	0.0926	58.77	6.0	300

Table 1. Simulation free-stream and wall conditions.

considered, $Re' = 11 \times 10^6$ m^{-1} and 22×10^6 m^{-1}. The free-stream and wall conditions used are presented in table 1. The incidence angle of the cone is set to zero in all but one of the computed base-flow solutions. In the one exception, a small yaw angle of 0.5° is imposed by deflecting the free-stream velocity vector in the $+Z$ direction. In all cases, Stokes' hypothesis (the second coefficient of viscosity $\lambda = -2\mu/3$) is assumed. Sutherland's law is used to calculate viscosity (μ)

$$\mu = \mu_{ref} \left(\frac{T}{T_{ref}} \right)^{3/2} \frac{T_{ref} + S_{ref}}{T + S_{ref}}, \tag{2.2}$$

with $S_{ref} = 110.556$ K, $T_{ref} = 273.111$ K, and $\mu_{ref} = 1.716 \times 10^{-5}$ kg (m s)$^{-1}$. Additionally, a constant Prandtl number (Pr) of 0.72 is assumed. The working fluid is air with a gas constant (R) of 287 J (kg K)$^{-1}$.

A structured mesh is generated using grid software provided by Pointwise. NASA's Data-Parallel Line Relaxation (DPLR) code is used to obtain the steady base-flow solutions (Wright, Candler & Bose 1998). In the cases with zero-incidence angle, the simulation costs are reduced by splitting the simulations into two parts. First, flow over the cone (excluding the fin) is modelled as axisymmetric. This grid uses 501 points in the streamwise direction and 351 points in the wall-normal direction. A second three-dimensional domain (beginning ∼16 mm upstream of the fin) overlaps with the axisymmetric domain and models half of the fin cone. The overlap is chosen to minimize any error from assuming an axisymmetric flow too close to the fin root, as well as to avoid interpolating too close to the outlet in the axisymmetric solution. (See Peck *et al.* 2022*b* for a detailed error analysis of this method.) The geometric symmetry line is used to reduce computational costs in the three-dimensional, zero-incidence-angle simulations. These three-dimensional grids use 785 streamwise, 606 wall-normal and 726 azimuthal grid points. The fin alone uses 354 grid points in the azimuthal direction. The convergence of the base flows was demonstrated in Middlebrooks *et al.* (2022) by examining the sensitivity of LPSE results to the base-flow grid density. In the one non-zero-yaw case, the

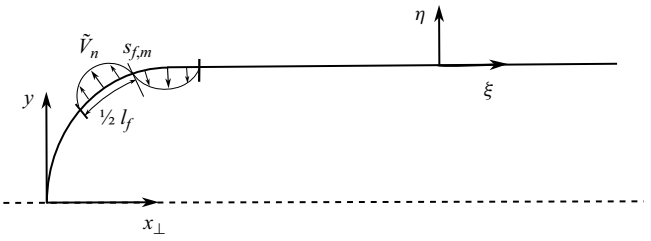

Figure 2. Stability domain coordinate system and wall-forcing variable definition. The solid line is the fin, the dashed line is the symmetry plane.

entire cone is simulated at once. The free-stream conditions are enforced at the upstream, outer boundaries of the simulation. The wall is modelled as isothermal ($T_{wall} = 300$ K, resulting in a mildly cooled wall, $T_{wall}/T_0 \sim 62.5\,\%$) and enforces no slip on the velocities. The outlet uses extrapolation conditions.

2.2. *Harmonic linearized Navier–Stokes equations*

For the stability analysis in this paper, the fin is analysed similarly to an infinite wing. The stability plane is oriented perpendicular to the leading edge and spanwise gradients are neglected. Analysis in Middlebrooks *et al.* (2022) demonstrates this is an acceptable assumption because the spanwise pressure gradient (banded between -0.5 and 0.5 kPa m^{-1}) is small compared with the streamwise pressure gradient (which has a maximum favourable gradient of $\sim$1050 kPa m^{-1}, and remains at least an order of magnitude larger than the spanwise gradient throughout the streamwise domain). Further evidence is provided in Middlebrooks *et al.* (2022) by comparing the LPSE results computed at 12 different spanwise stations. Results were qualitatively similar in all cases and quantitatively similar in stations 5–12 (the current HLNS domain is equivalent to the LPSE station 6). Finally, neglecting the spanwise gradients is justified *a posteriori* through the observation of a quasi-spanwise-uniform transition front in experiments by Middlebrooks *et al.* (2022). This indicates that disturbances grow in the direction perpendicular to the leading edge; growth parallel to the leading edge can be neglected. These observations justify neglecting spanwise derivatives of the base-flow variables and, in turn, this allows imposing a purely oscillatory perturbation in the spanwise direction and time. Lastly, we are specifically interested in perturbations that emerge as a consequence of forcing at the wall. These assumptions are most generally captured by the HLNS equations (see Guo, Malik & Chang 1997; Malik, Lin & Sengupta 1999). We enforce that the perturbation takes the form

$$q'(\xi, \eta, \zeta, t) = \tilde{q}(\xi, \eta) \exp[\mathrm{i}(\beta\zeta - \omega t)], \tag{2.3}$$

where (ξ, η) are defined in figure 2 and ζ completes the system. Note that in this case, ζ points upstream, i.e. it has a component in the $-X$ direction. The constants β (spanwise wavenumber) and ω (angular frequency) are real and prescribed for the problem.

Equation (2.3) is substituted into the linearized Navier–Stokes equations. The resulting equations are expressed in matrix form as an operator on a state vector $\tilde{\boldsymbol{q}}$:

$$\tilde{\boldsymbol{q}} = [\tilde{u}, \tilde{v}, \tilde{w}, \tilde{T}, \tilde{\rho}]^{\mathrm{T}}. \tag{2.4}$$

The individual terms are grouped together in the following way to facilitate simple parameter sweeps through (β, ω):

$$\underbrace{(\boldsymbol{A} + \beta\boldsymbol{B} + \omega\boldsymbol{C} + \beta^2\boldsymbol{D})}_{\boldsymbol{M}}\tilde{\boldsymbol{q}} = \boldsymbol{f}. \tag{2.5}$$

The vector $\boldsymbol{f}$ is a prescribed forcing function at the wall. The matrices $\boldsymbol{A}$–$\boldsymbol{D}$ contain basic-state variables and derivatives, as well as discretized derivative operators acting on $\tilde{\boldsymbol{q}}$. The matrix $\boldsymbol{M}$ is inverted using MUMPS (MUltifrontal Massively Parallel sparse direct Solver) to solve for $\tilde{\boldsymbol{q}}$ (Amestoy *et al.* 2001, 2019). The in-house HLNS code is verified in Peck, Groot & Reed (2022*a*).

The stability grids are built in Pointwise. The symmetry plane and fin surface mark where $\xi = 0$ and $\eta = 0$, respectively. The free-stream boundary is cropped to remove the shock from the stability domain. The disturbances examined in this paper propagate through the boundary layer and do not interact with the shock, which justifies removing it from the stability domain. The streamwise extent ends prior to the change in fin thickness seen in figure 1. This encompasses the transition front observed at the experiment's highest unit Reynolds number. The grid has 701 points in the streamwise direction and 586 points in the wall-normal direction. Sixth-order finite differences are used to approximate streamwise and wall-normal derivatives. Details on grid convergence and other numerical studies are presented in Appendix A.

Boundary conditions are prescribed within $\boldsymbol{M}$ and $\boldsymbol{f}$. The perturbation velocities at the wall are set to zero (excluding inside the forcing region, labelled l_f in figure 2, where $\tilde{u}$ and $\tilde{v}$ are non-zero to enforce the required normal velocity, $\tilde{v}_n$). The temperature perturbation at the wall is always constrained to zero, also for stationary perturbations. This is justified due to the short wind-tunnel run time in the experiments from which the present conditions were derived. The density perturbation is solved for at the wall using a compatibility condition based on the continuity equation. Symmetry is enforced at the symmetry plane. To avoid spurious reflections, the free stream and outlet use a combination of non-reflecting boundary conditions (see Thompson 1987; Jiang *et al.* 1999) and a buffer (similar to Meitz & Fasel 2000). Appendix A details the buffer method and demonstrates independence from buffer effects. No special consideration is given to the effect of shocks, as the stability domain is always constrained below any shocks.

Wall suction/blowing is used to excite boundary-layer perturbations, as multiple studies have demonstrated that hypersonic boundary layers are very receptive to it (e.g. Fedorov & Khokhlov 2002). In order to excite disturbances with similar characteristics to those seen in experiments, a sinusoidal forcing function is applied to the wall-normal velocity shape function. The function is

$$\tilde{v}_n = \left[\sin\left(\frac{2\pi s_f}{l_f}\right) - \mathrm{i}\cos\left(\frac{2\pi s_f}{l_f}\right)\right]\left(\frac{4(s_f)(s_f + 2s_{f,m} - l_f)}{l_f^2}\right)^3, \tag{2.6}$$

where l_f is the prescribed streamwise extent of the forcing function and s_f (the surface distance inside the forcing region) is constrained from 0 to l_f; $s_{f,m}$ denotes the middle of the forcing function, measured as a surface distance starting from the symmetry plane. The forcing wave function, specifying the frequency and spanwise wavenumber of the prescribed forcing, matches the assumed frequency and spanwise wavenumber of the solution. Here, $s_{f,m}$ is fixed at 5 mm unless otherwise noted. Varying both β and l_f changes the angle between the simulation plane and the axis of the forcing 'streaks'. Unless otherwise noted, simulations fix the axis of the forcing streaks to -70°, which

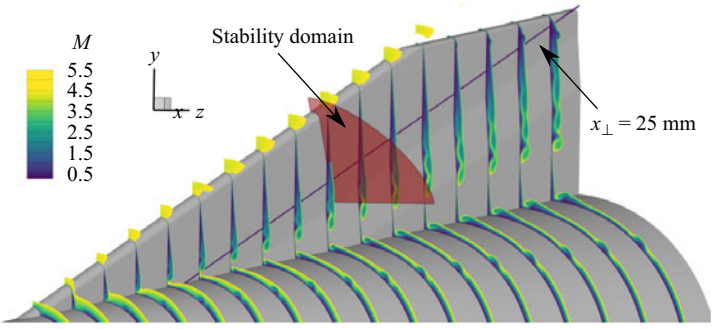

Figure 3. Mach contours (cropped above $M = 4.5$ for visibility) at $Re' = 11 \times 10^6$ m^{-1}. The stability domain is included for reference, along with a line marking $x_\perp = 25$ mm.

approximately aligns the forcing with the direction of the free-stream flow. As a result, l_f is made dependent on β

$$l_f = \frac{2\pi}{\beta \tan(70^\circ)}. \tag{2.7}$$

This study focuses on -70° forcing so that the simulations excite cross-flow-like disturbances in particular. Some experimentation indicated this forcing configuration is suitable for that purpose.

3. Stability analysis

This section presents the stability characteristics of disturbances at $Re' = 11 \times 10^6$ m^{-1}. The laminar base flow is briefly reviewed. The presence of the fin disrupts the axisymmetric flow on the cone surface and produces a shock at the fin root. The pressure gradients produced by the fin are large enough to induce multiple vortices: one on the surface of the cone, moving outboard as the flow moves downstream, another on the fin moving away from the surface of the cone, and a third in the corner formed by the fin and cone. These vortices are highlighted in the Mach contours shown in figure 3. The fin vortex moves away from the surface of the cone as the flow moves downstream. This paper focuses on disturbance growth in the region between the leading edge and the start of the fin vortex.

The stability frame is oriented perpendicular to the leading edge, as in an infinite swept wing analysis. One plane of data is taken where the origin of the new $(x_\perp, y)$ system (see figure 2) corresponds to $(X_G, Y_G, Z_G) = (0.291, 0.089, 0)$. The base-flow velocities are rotated to align with the new coordinate system. The new 'streamwise' and 'spanwise' components (i.e. components perpendicular and parallel to the leading edge, respectively) are identified with a subscript $\perp$ to disambiguate from other coordinate systems used in this paper. After rotating the data to the stability plane, the largest component of base-flow velocity is $\overline{W}_\perp$, which is shown in figure 4. An additional effect of the rotation is that parts of the flow near the wall now contain reversed flow ($\overline{U}_\perp < 0$; these regions' boundaries are outlined in white in figure 4). Any potential elliptical effects caused by the 'upstream' flow will be captured by HLNS.

Forcing is applied for a range of wavelengths in the range $\lambda_\parallel \in [3, 15]$ mm, where $\lambda_\parallel = 2\pi/\beta$ is the spanwise wavelength, i.e. in the direction parallel to the leading edge. The wavelength parameter space is broken in increments of 0.25 mm between 3 and 7 mm and increments of 1 mm above 7 mm. The boundary layer is receptive to the applied wall

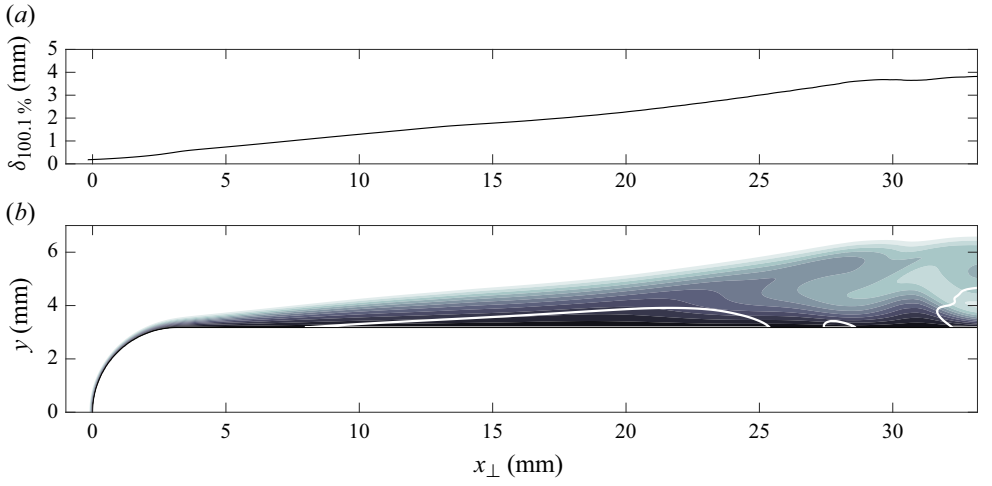

Figure 4. Boundary-layer thickness (a) and contours of $\overline{W}_\perp$ (b) for $Re' = 11 \times 10^6$ m^{-1}. The white line indicates regions where $\overline{U}_\perp$ is negative. The contours are equally spaced between 0 and -875 m s^{-1}.

forcing and regular, wave-like disturbances grow downstream. The disturbance growth is quantified using the Chu-energy description, described in Hanifi, Schmid & Henningson (1996)

$$E = \int \tilde{\boldsymbol{q}}^H \overline{\boldsymbol{C}} \tilde{\boldsymbol{q}} \, \mathrm{d}y, \tag{3.1}$$

where $\tilde{\boldsymbol{q}}$ is defined in (2.4), H indicates Hermitian transpose and

$$\overline{\boldsymbol{C}} = \mathrm{diag}\left(\overline{\rho}, \overline{\rho}, \overline{\rho}, \frac{\overline{\rho}}{\gamma(\gamma-1)M^2\overline{T}}, \frac{\overline{T}}{\gamma M^2 \overline{\rho}}\right). \tag{3.2}$$

Here, M is the Mach number (based on $\overline{U}_\perp$) and γ is the ratio of specific heats ($\gamma = 1.4$). The amplification factor, or N-factor (N_E), uses the maximum energy within the forcing region, $E_{max,f}$, as a reference for the growth within the domain

$$N_E = \frac{1}{2} \ln \frac{E}{E_{max,f}}. \tag{3.3}$$

Figure 5(a) shows the N-factors for several wavelengths. All wavelengths within the range examined are amplified. The most-amplified wavelength is 5 mm, with $N_E = 3.47$ at $x_\perp = 25$ mm. This is relatively low ($\sim 32x$ amplification of initial amplitudes), suggesting that nonlinear effects may not be important except in scenarios with large initial disturbances. The 5 mm wave becomes locally the most-amplified by $x_\perp = 18$ mm. Between $x_\perp = 6$ and 18 mm, the 5 mm amplification is nearly equal to the 4.5 mm wave. Smaller wavelengths appear to only be unstable near the leading edge, while large wavelengths grow over the entire domain, but less so than the 5 mm case.

The parameter space is broadened to include unsteady disturbances. Simulations are run in 5 kHz and 1 mm increments. Due to the coordinate system, where $z_\perp$ points upstream, the most unstable quadrant is $[+\omega, -\beta]$ (or, equivalently, $[-\omega, +\beta]$), however, plot labels are given as $(f, \lambda_\parallel)$ with any signs removed for clarity, where $f = \omega/(2\pi)$ is the cyclic frequency. Figure 5(b) shows N_E for the entire space at $x_\perp = 25$ mm. The most-amplified

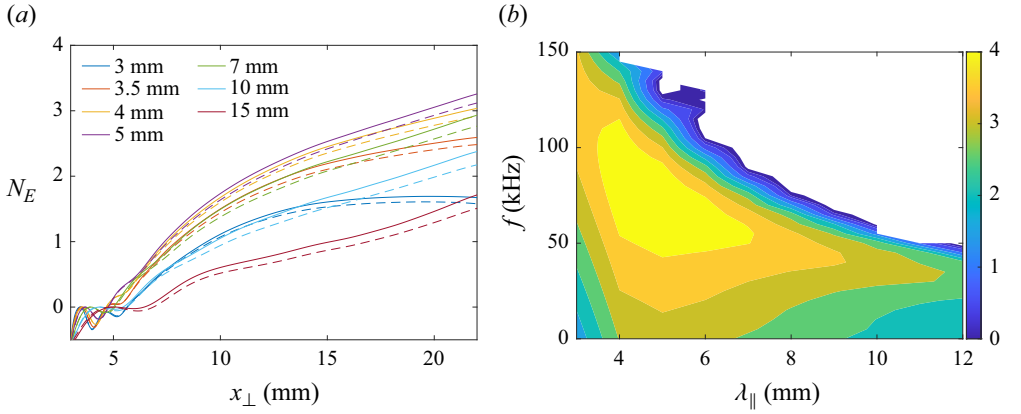

Figure 5. The N-factors (based on Chu energy) for disturbances at $Re' = 11 \times 10^6$ m^{-1}. Panel (*a*) shows the N-factor along the entire domain for stationary disturbances only (solid lines). Dashed lines use a modified N-factor definition (see § 4). Panel (*b*) shows the N-factor measured at $x_\perp = 22$ mm for all disturbances.

disturbance is the 5 mm wave at 75 kHz with an N-factor of 4.99. The highly amplified region is centred around 4–6 mm and 50–100 kHz. As the wavelength increases, the most-amplified frequency decreases. Note the frequency space for each wavelength is limited to capturing only the frequency with the largest N_E. Increasing the frequency much further past this point was found to be subject to buffer effects.

To better characterize the disturbances, the inviscid streamline frame is defined (important quantities are shown in figure 6). The boundary-layer edge is quantified using total enthalpy, h,

$$h = c_p \overline{T} + \tfrac{1}{2}|\overline{U}|^2. \tag{3.4}$$

When h/h_0 (h_0 is the free-stream total enthalpy) reaches an overshoot value of 100.1 % for the first time, moving from the free stream towards the wall, the boundary-layer edge ($\delta_{100.1\,\%}$, shown in figure 4) is marked. At this location, the inviscid free-stream direction, ϕ, is quantified

$$\phi = \tan^{-1} \frac{\overline{W}_\perp}{\overline{U}_\perp}. \tag{3.5}$$

Above the flat portion of the fin, ϕ varies slightly between $-71°$ and $-74°$. With the inviscid free-stream direction quantified, the base-flow profiles can be rotated in the direction of the inviscid streamline. In this coordinate system, $\overline{U}_s$ is aligned with the inviscid streamline and $\overline{W}_{cf}$ is the cross-flow component.

The disturbance structure for the most-amplified stationary disturbance is shown in figure 7 using the real part of the temperature disturbance, $\mathcal{R}(\tilde{T})$. The disturbance tends to remain in a shear layer between the top edge of the boundary layer (indicated with the solid line off of the wall) and the location where $\overline{W}_{cf} = 0$ (dashed line). This shear layer rises with the growing boundary layer and lifts the disturbance away from the wall and reversed-flow region (dash-dotted line). Smaller wavelengths tend to be more concentrated in this layer and large wavelengths have a structure that stretches outside of this shear layer and deeper into the boundary layer. This idea will be returned to in later sections.

Figure 7 demonstrates that the disturbance has a wave-like structure. Although HLNS does not enforce a streamwise wavelength, it may be extracted by interpolating some

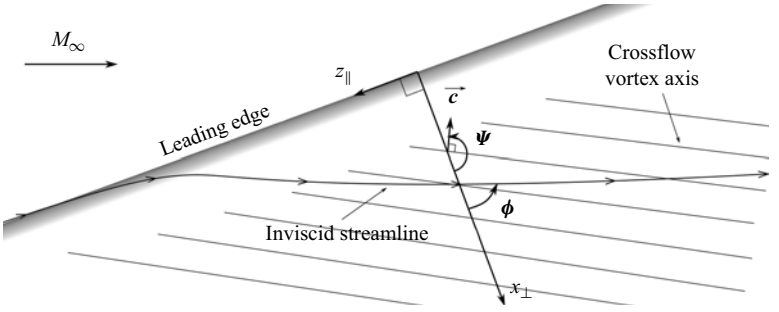

Figure 6. A side view of the fin (flow is from left to right) defining the angles between the stability frame ($x_\perp, z_\parallel$) and inviscid streamline (ϕ), and the angle between the stability frame and cross-flow wave vector (ψ). Both ϕ and ψ, as drawn, are negative.

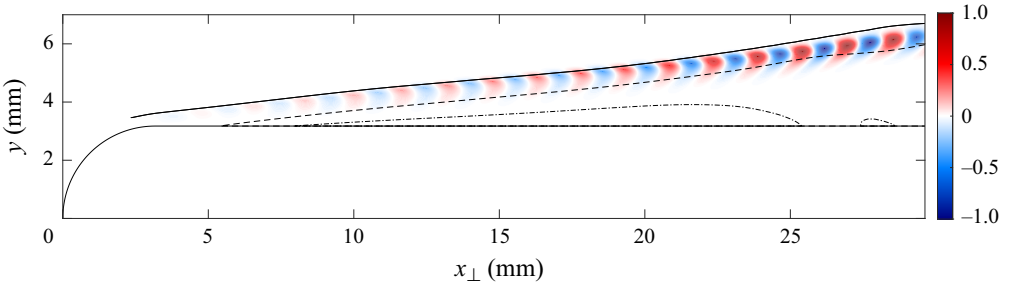

Figure 7. Disturbance ($f = 0$ kHz, $\lambda_\parallel = 5$ mm) visualized using $\mathcal{R}(\tilde{T})/\max|\tilde{T}|$. Lines mark the boundary-layer edge (solid), reversed flow (dash-dotted) and $\overline{W}_{cf} = 0$ (dashed).

quantity (we chose $\tilde{\rho}$) along the sonic line, which nearly aligns with the local maximum in the perturbation shape functions. The distance between the zeros of $\mathcal{R}(\tilde{\rho})$ is marked as half a streamwise wavelength and the conversion to α_r (where the subscript r indicates the real part) is made. The wave angle, ψ, of the disturbance is then quantified, along with the phase speed, $\vec{c}$

$$\psi = \tan^{-1}\frac{\beta}{\alpha_r}, \tag{3.6}$$

$$\vec{c} = \frac{\omega}{\alpha_r^2 + \beta^2}(\alpha_r, 0, \beta). \tag{3.7}$$

The wave angle and phase-speed magnitude are shown in figure 8 for several wavelengths. In all cases, both quantities are practically constant across the streamwise extent of the domain. Presented results are thus averaged over the domain to provide a single data point for each (f, $\lambda_\parallel$) pair. For the stationary disturbances, ψ is nearly constant and at $\sim 90^\circ$ offset from the inviscid streamline direction, ϕ, for all wavelengths examined (recall $\phi \sim -70^\circ$). In a few cases, the cross-flow vortex axis crosses over the inviscid streamline as the flow moves downstream (e.g. the stationary 10 mm wave). At higher frequencies, the wave angle is more dependent on the disturbance wavelength. For all wavelengths, as the frequency increases the wave vector gradually rotates towards the inviscid streamline direction. As the wavelength increases, this rotation begins at lower frequencies. Additionally, the phase speed increases more rapidly at smaller frequencies for larger wavelengths. The most unstable travelling disturbance ($\lambda_\parallel = 5$ mm,

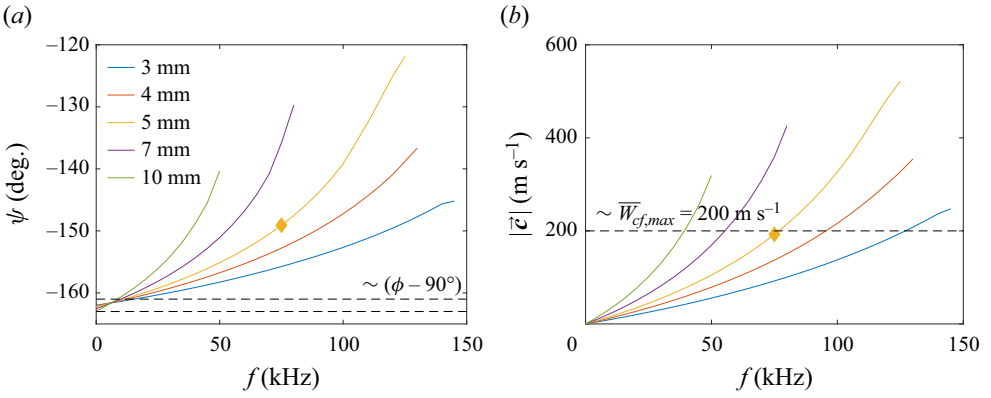

Figure 8. Disturbance characteristics averaged over the streamwise domain at $Re' = 11 \times 10^6$ m^{-1}. The most-amplified wave is indicated with a diamond marker. In (*a*), the range of the inviscid streamline angle is marked with black dashed lines. (*a*) Wave angle and (*b*) phase speed.

$f = 75$ kHz) has a wave angle of $-149°$ and a phase speed of 192 m s^{-1}, or approximately $0.21U_\infty$, where U_∞ is the free-stream velocity ($\sim$920 m s^{-1}). The phase speed of the most-amplified wave is very close to the maximum cross-flow velocity measured in the domain ($\sim$200 m s^{-1}); this is expected in light of the approximate alignment of the wave vector with the direction of the cross-flow velocity component.

3.1. *Effect of forcing location and angle*

A brief study of the effect of forcing location, $s_{f,m}$, and angle (directly affecting l_f) is performed. First, several forcing locations are chosen ranging between $s_{f,m} = 3$ and 11 mm. Note that when forcing at $s_{f,m} = 11$ mm, the entire forcing region overlaps with the backflow region. The forcing location's effect on disturbances is only examined for stationary perturbations.

Representative N-factors are shown in figure 9(*a*). In order to infer that the same mode is excited regardless of the forcing location, the slope of the lines is examined. For the 10 mm wave, the slope of the lines appears to be approximately equal regardless of the forcing location. This indicates that the same mode is excited in all cases by the wall-forcing function. For smaller wavelengths, the growth rate appears equal only for the upstream forcing locations. When forcing at $s_{f,m} = 9$ or 11 mm, the 3.5 mm mode discussed in the above sections is not excited by the wall forcing. There is practically no growth downstream of the forcing location. The 5 mm mode is still unstable when forced at $s_{f,m} = 9$ or 11 mm, but is less amplified than the 10 mm wave.

These trends follow the observations made in the previous section. The small-wavelength disturbances, when excited, have a strong signature in the shear layer above the sonic line. While the shear layer, which has the length scale necessary to support small wavelength disturbances, exists in all streamwise locations, downstream of the leading edge the shear layer is apparently too far from the wall to be strongly affected by wall forcing. Conversely, the 10 mm wave occupies a larger extent of the boundary layer and is not too separated from the wall to be immune to wall forcing. This demonstrates that the streamwise region of receptivity to wall forcing is extensive for large-wavelength disturbances. Smaller-wavelength disturbances must be excited around the leading edge. An adjoint analysis could fully define the optimal receptivity locations for the different

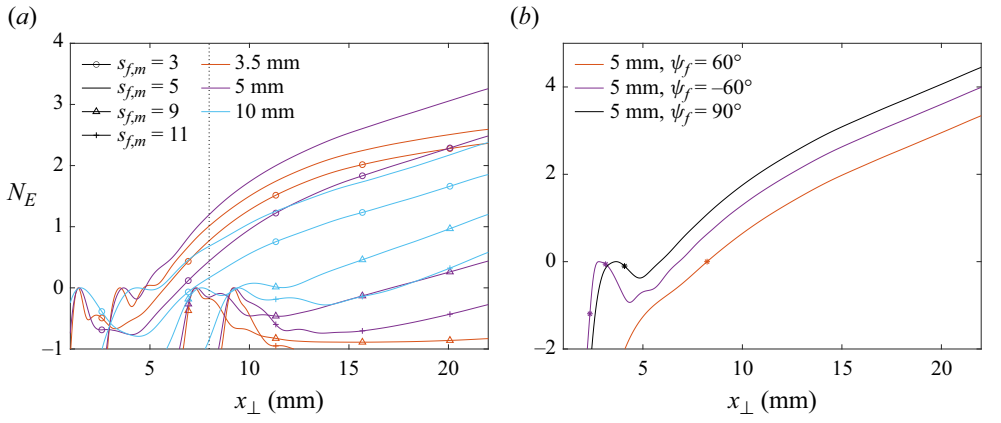

Figure 9. The N-factors (based on Chu energy) for stationary disturbances at $Re' = 11 \times 10^6$ m^{-1} while varying the forcing function parameters $s_{f,m}$ and l_f. In (*a*), different colours and line styles indicate different spanwise wavelengths and forcing locations, respectively. The vertical dotted line marks the start of the reversed-flow region. In (*b*), different colours indicate different forcing angles, ϕ_f, related to the streamwise forcing length, l_f. Asterisks on the lines denote the extent of the forcing region. All forcing regions in this case are aligned at the start of the forcing region.

disturbances, however, this is beyond the scope of the present study. Finally, the lack of growth for small-wavelength disturbances in the cases of downstream forcing suggests there is either no secondary unstable mode in the spectrum that would exist closer to the wall, or, if one does exist, it is not at all receptive to the wall forcing used in this study.

The second study considers the effect of changing the forcing angle, which is related to the streamwise length of the forcing region, l_f, based on a fixed spanwise wavelength. Specifically, we examine the effect of 'first-mode-like' forcing, where the forcing wave angle is designed to be approximately $\pm 60^\circ$ with respect to the inviscid streamline. To achieve this, the angle in (2.7) is changed to 40° and 80°, respectively. We test this forcing on the most unstable travelling wave for these conditions, which is the 5 mm wave at 75 kHz, with the expectation that this wavelength and frequency would be in the range of an unstable first mode if it exists. The results from this study are shown in figure 9(*b*). The orange and purple lines, measuring the response from attempting to force a first mode, match very well with the growth rate recovered from forcing cross-flow-like disturbances (the black line). The forcing angle therefore does not appear to have a large effect on the results presented.

3.2. *Amplification based on wall quantities*

Large-wavelength disturbances were previously noted to stretch outside of the shear layer, that is located between the boundary-layer edge and where $\overline{W}_{cf} = 0$, and propagate towards the wall. This raises the question of to what extent the reversed-flow region influences the perturbation. To help answer this qualitatively, the disturbance structure for several stationary wavelengths is shown in figure 10, this time with levels of $\mathcal{R}(\tilde{T})$ on a log scale to highlight features within the reversed-flow region. It is apparent that small-wavelength disturbances are attenuated in the reversed-flow region, but it more readily supports large-wavelength disturbances. These results are qualitatively similar to a study investigating three-dimensional disturbances passing through a laminar separation bubble at incompressible speeds (see figure 21 in Hosseinverdi & Fasel 2016).

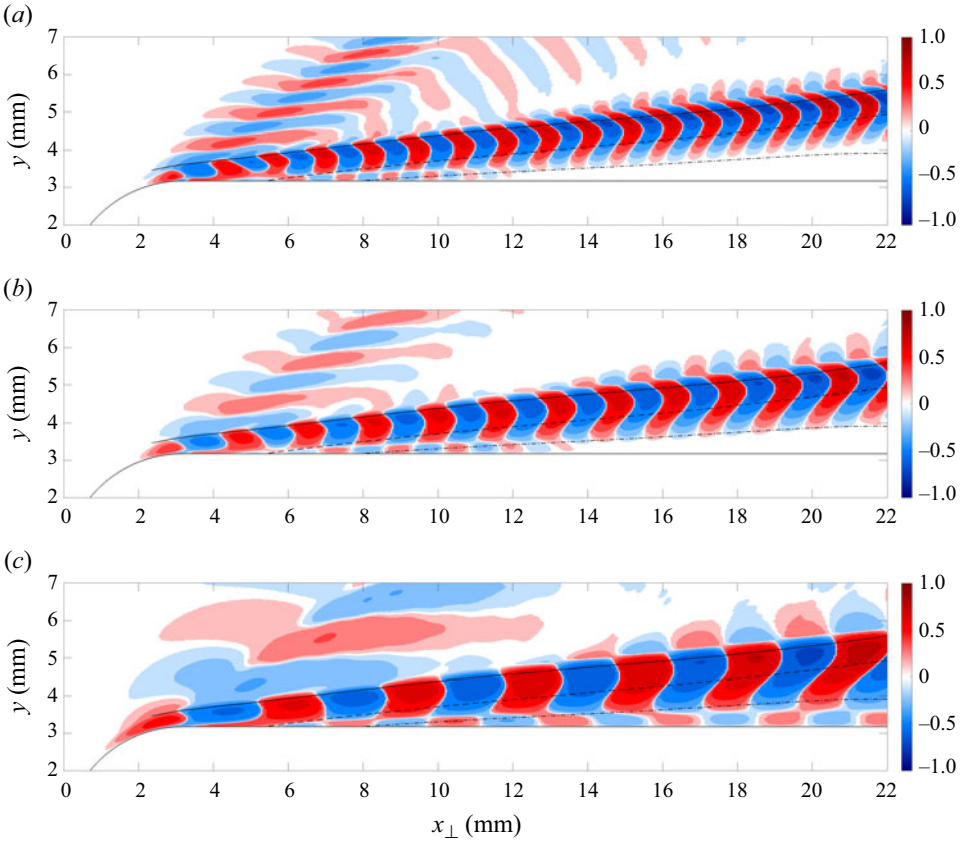

Figure 10. Disturbances ($f = 0$ kHz) visualized using $\mathcal{R}(\tilde{T})/\max|\tilde{T}|$ on a logarithmically spaced scale (10^{-4}–10^{0}) (colour contours). Lines mark the boundary-layer edge (solid), reversed flow (dash-dotted) and $\overline{W}_{cf} = 0$ (dashed). Panels show (*a*) $\lambda_\parallel = 3.5$ mm, (*b*) $\lambda_\parallel = 5$ mm and (*c*) $\lambda_\parallel = 10$ mm.

It is reasonable to suspect the reversed-flow region may produce upstream travelling disturbances. Recall the above measured phase speeds measured along the sonic line, which always resides above the reversed-flow region and could miss any upstream perturbations that reside in the reversed flow. With this in mind, the phase lead/lag of the disturbances was carefully examined in the reversed-flow region to look for possible negative phase speeds in the $x_\perp$ direction, but none were found. The log scale used in figure 10 also highlights free-stream waves emitted from the boundary layer due to the forcing. These emissions represent a small ejection of energy from the boundary layer into the free stream, rather than all of the energy from the forcing being directed into the boundary layer.

The increased presence of the large-wavelength structures near the wall raises additional questions on how any wind-tunnel measurements based solely on wall quantities may be biased. To help answer this question, additional amplification factors are defined based purely on wall quantities and inspired by experimental measurement techniques. Specifically, the wall heat flux and pressure are quantified and their 'amplification' (N_{q_w} and N_{p_w}, respectively) is measured in reference to the maximum value inside the forcing

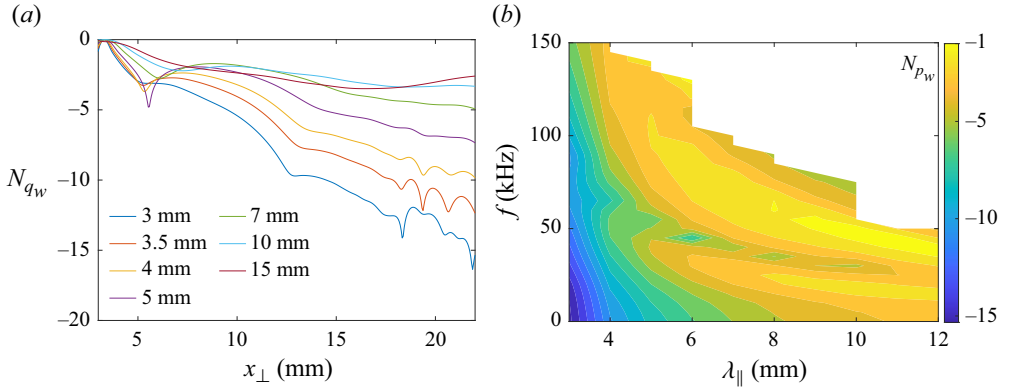

Figure 11. The N-factors for disturbances at $Re' = 11 \times 10^6$ m^{-1}. (*a*) Shows the N-factor based on wall heat flux (N_{q_w}) along the entire domain for stationary disturbances only. (*b*) Shows the N-factor based on wall pressure (N_{p_w}) measured at $x_\perp = 25$ mm for all disturbances. (*a*) $f = 0$ kHz, (*b*) $x_\perp = 22$ mm.

region, similar to N_E. The perturbed wall heat flux is derived using

$$q'_w = (\kappa \nabla T \cdot \hat{\boldsymbol{n}})' = \frac{\mathrm{d}\overline{\kappa}}{\mathrm{d}T} T' (\nabla \overline{T} \cdot \hat{\boldsymbol{n}}) + \overline{\kappa} (\nabla T' \cdot \hat{\boldsymbol{n}}), \tag{3.8}$$

where $\hat{\boldsymbol{n}} = (\hat{n}_{x_\perp}, \hat{n}_y, 0)$ is the outward unit normal with respect to the wall. The perturbation ansatz is substituted and the expression simplified using the boundary condition $\tilde{T}_w = 0$

$$\tilde{q}_w = \overline{\kappa} \left(\left. \frac{\partial \tilde{T}}{\partial x_\perp} \right|_w \hat{n}_{x_\perp} + \left. \frac{\partial \tilde{T}}{\partial y} \right|_w \hat{n}_y \right). \tag{3.9}$$

The $\hat{n}_{x_\perp}$ term is necessary to include the curved leading edge. The wall pressure, $\tilde{p}_w$, is derived from the non-dimensional equation of state

$$\gamma M^2 \overline{P} = \overline{\rho} \overline{T}, \tag{3.10}$$

$$\tilde{p}_w = \overline{P} \left(\frac{\tilde{\rho}_w}{\overline{\rho}} + \frac{\tilde{T}_w}{\overline{T}} \right) = \frac{\overline{T} \tilde{\rho}_w}{\gamma M^2}, \tag{3.11}$$

where the final expression for $\tilde{p}_w$ follows from again enforcing $\tilde{T}_w = 0$ for all cases.

The value of N_{q_w} is only examined for stationary disturbances and is shown in figure 11(*a*). All wavelengths exhibit a reduction in N_{q_w} immediately downstream of the forcing location. This follows from the perturbation lifting up off the wall with the growing boundary layer. However, the drop off is most extreme for the small wavelengths. The largest wavelength shows a small increase in N_{q_w} within the recirculation region which is explained by the behaviour of the $\tilde{T}$ structures pointed out in figure 10. Basing a 'most-amplified' judgement on N_{q_w} values results in a much larger estimate of 15 mm, which is 10 mm larger than the N_E most-amplified disturbance. Note that, because the N-factors are negative due to amplitude decay, 15 mm is technically the least-damped disturbance. However, these disturbances are still referred to as 'most amplified' to retain consistent terminology with the total-energy N-factor.

A similar trend is seen in N_{p_w}, measured for all travelling disturbances and shown in figure 11(*b*). Based on wall quantities, very different frequencies are found to be most

amplified vs the measurement using the Chu norm. The most-amplified wavelengths of unsteady disturbances are between 9 and 12 mm, and have a lower-frequency band of 35–55 kHz, vs the previously quoted 75 kHz based on the Chu norm. Note that the perturbation wall pressure occasionally drops to zero in very localized regions. The exact spot where the pressure becomes zero depends on the disturbance wavelength and frequency. Due to this zero point, the N-factor in figure 11(b) appears to have two peaks. However, these two peaks would become one smoothly defined region if the probe is shifted slightly, so we do not interpret distinct behaviour between these two peaks. Using heat flux and wall pressure as two alternative measurements of perturbation amplification presents evidence of a significant bias towards large wavelengths and low frequencies when only collecting flow information at the wall. This is due to the rapidly growing boundary layer drawing the disturbances away from the wall.

3.3. *Discussion on perturbation classification*

Thus far, we have refrained from categorizing the simulated disturbances as the result of a particular type of instability. If we combine the highly swept fin, large cross-flow velocities in the base flow, and some key disturbance characteristics (such as wave angles that are nearly perpendicular to the inviscid streamline), this study appears at first glance to be on the traditional cross-flow instability. However, other characteristics of this case defy traditional expectations for cross-flow instability behaviour, and we believe this warrants further discussion before firmly classifying the disturbances. The various pieces of evidence for and against cross-flow are discussed here.

To aid in the present discussion, some base-flow profiles are examined in figure 12. All profiles have been rotated into the inviscid streamline frame. The largest cross-flow component is found at $x_\perp = 3.175$ mm, where the fin first transitions from the circular leading edge to the flat side of the plate. The value of $\overline{W}_{cf,max}$ at this location is $\sim$200 m s^{-1}, or $\sim 0.22U_\infty$. This is an extremely large cross-flow velocity relative to other examples in the literature that investigate cross-flow. While not often directly reported, examples include Liu (2022), who studies a series of Falkner–Skan–Cooke boundary layers with a maximum cross-flow velocity of 8 % in Mach 4.5 flow, and Chen *et al.* (2022*b*), who report the maximum cross-flow velocity as $\sim$7.5 % in their case studying high-enthalpy boundary layers in Mach 16 flow over a swept parabola. As an extreme case, Mack (1984) gives an incompressible example where cross-flow instability occurs when the cross-flow velocity is as small as 0.7 % of U_∞. These examples raise expectations that the present case must surely feature the cross-flow instability.

Due to the complex underlying base flow, the traditional cross-flow profiles like the one observed in figure 12(a) only exist for a short streamwise distance. The remaining figures illustrate how the profiles develop qualitative changes farther downstream. First, the thickening boundary layer causes the maximum in cross-flow velocity to move away from the wall. Additionally, by $x_\perp = 8$ mm, the adverse pressure gradient in the $x_\perp$ direction causes a secondary cross-flow lobe to appear in the opposite direction. This secondary lobe continues to grow as the flow moves away from the leading edge, and eventually the secondary cross-flow has a larger peak velocity than the first lobe, which continues to exist high in the boundary layer.

This is a similar situation to the low-speed case examined by Wassermann & Kloker (2005), where a changeover from favourable to adverse pressure gradients also caused S-shaped cross-flow velocity profiles. In that case, linear stability theory results indicated

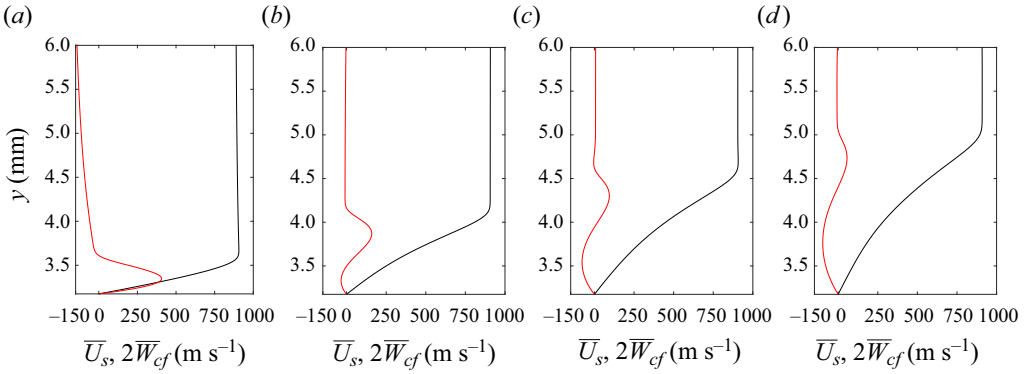

Figure 12. Rotated base-flow profiles at $Re' = 11 \times 10^6$ m^{-1}. Shown are the streamwise (black) and cross-flow (red) velocities. The cross-flow velocities are doubled to improve visibility. Panels show (*a*) $x_\perp = 3.175$ mm, (*b*) $x_\perp = 8$ mm, (*c*) $x_\perp = 12.5$ mm and (*d*) $x_\perp = 17.5$ mm.

that, in the adverse pressure gradient region, the range of unstable cross-flow wavenumbers and cross-flow growth rates were reduced (compared with within the favourable pressure gradient region), and first-mode instabilities became more strongly amplified instead. Based on the forcing parameter study presented in § 3.1, the present case does not seem to produce first-mode instabilities. However, based on the incompressible results shown by Wassermann & Kloker (2005), one might still expect to see a significant impact on the growth rate of a cross-flow mode due to the changeover in pressure gradients. This does not seem to be the case when considering the N-factors shown in figure 5(*a*). A possible interpretation is that the upper cross-flow lobe isolates the disturbances from the effect of the pressure gradient changeover. Rather, the pressure gradient changeover effects are more dominant over the behaviour of disturbances closer to the wall. This view will be examined more through an energy budget lens presented in the next section.

The S-shaped boundary-layer profiles towards the end of the streamwise domain therefore cast some doubt on calling the disturbances shown in the previous sections 'true cross-flow instabilities'. The secondary cross-flow lobe represents a significant departure from the classic cross-flow profile with a single maximum in cross-flow velocity, and indeed, the base-flow cross-flow velocity becomes dominant closer to the wall where the (most-amplified) instabilities appear highly damped. However, the large cross-flow velocity near the leading edge and the fact that the (most-amplified) disturbances are highly destabilized in the region in the range $x_\perp = 5$–10 mm, where the original cross-flow lobe is dominant, suggest that the most-amplified disturbances may originate as a result of the cross-flow instability. The driving mechanisms of the disturbance evolution downstream, as well as the behaviour of the large-wavelength disturbances, is less clear from an analysis of base-flow profiles alone.

One might propose separating the disturbances shown in the present paper into two categories based on the underlying instability. The first category concerns the small wavelengths (encompassing the most-amplified disturbances), which appear well categorized as unstable due to the cross-flow instability. These wavelengths are most unstable (see the N-factor slopes in figure 5*a*) in the region of flow where the classic cross-flow profile dominates, their wave angle and phase speed align well with other cross-flow examples in the literature, and the disturbance signature stays confined to the shear layer in the vicinity of the first maximum in cross-flow velocity. A second, currently

unlabelled category is reserved for the large wavelengths, which become appreciably unstable near $x_\perp = 8$ mm. These disturbances arise after the classic cross-flow profile has disappeared, and have a large enough extent through the boundary layer to be influenced by both cross-flow lobes. They are distinguished by their stronger wall signature.

It is difficult to declare an exact wavelength where the two groups could be considered without overlap, given the smooth variation between wavelengths. This is similar to the study presented by Liu (2022) where, even in simplistic Falkner–Skan–Cooke flow, cases arose where no clear distinction could be made between the first mode and cross-flow instabilities. It is also possible that both instabilities, the cross-flow instability and the currently unidentified 'large-wavelength' instability, could coexist at all wavelengths, and one instability is simply dominant over the other for different wavelengths. For now, we simply recognize the distinct characteristics that seem to dominate the small- and large-wavelength groups and caution against assuming cross-flow-like behaviour for the entire wavelength band. Finally, we note that we consider the underlying cause of instability to be separate from the driving mechanisms for growth, which are examined using an energy-budget analysis in the following section.

4. Energy analysis

The results presented so far raise a few questions. First, why is the 5 mm wave linearly most amplified according to the Chu-energy measurement? What physical processes are responsible for the growth, and why are other wavelengths not equally amplified? Next, a clear distinction is observed near the wall for small and large wavelengths. Why do large wavelengths propagate deeper into the boundary layer and why do small wavelengths remain confined to the shear layer? A related question is on why the temperature perturbation is able to grow inside the reversed-flow region for the large wavelengths only? Finally, what is the dominant mechanism providing energy to the perturbations, and does that line up with expectations for the cross-flow instability? To answer these questions, an energy budget is formulated for the spatial HLNS equations.

The goal of this section is to identify individual terms in the governing equations that are responsible for the disturbance growth; this will enable discovering the physical mechanisms that yield the amplification of perturbation energy. For now, we will restrict our definition of growth to one based on the Chu-energy norm. The N-factor definition is slightly modified to include an extra factor of $\overline{U}_\perp$. This is done so that the terms that appear in the upcoming growth definition ($\partial N_{\overline{U}}/\partial x$) exactly match terms that can be formed using the conservation equations. The N-factor is now defined as

$$N_{\overline{U}} = \frac{1}{2}\ln \int \tilde{\boldsymbol{q}}^H (\overline{U}_\perp \overline{\boldsymbol{C}}) \tilde{\boldsymbol{q}}\, \mathrm{d}y, \tag{4.1}$$

where $\boldsymbol{q}$ and $\overline{\boldsymbol{C}}$ were previously defined in (2.4) and (3.2), respectively. The additional $\overline{U}_\perp$ factor premultiplying $\overline{\boldsymbol{C}}$ produces only minor changes in the N-factor (see the dashed lines in figure 5*a*). The most-amplified wavelength remains unchanged. The quantity is no longer an energy, but, given the similar behaviour, it allows establishing the physical mechanisms underlying the perturbation amplification in space. To form the local growth rate, the x-derivative of the modified N-factor is expanded. The terms on the right-hand side are grouped into contributions from the perturbations (weighted according to Chu's

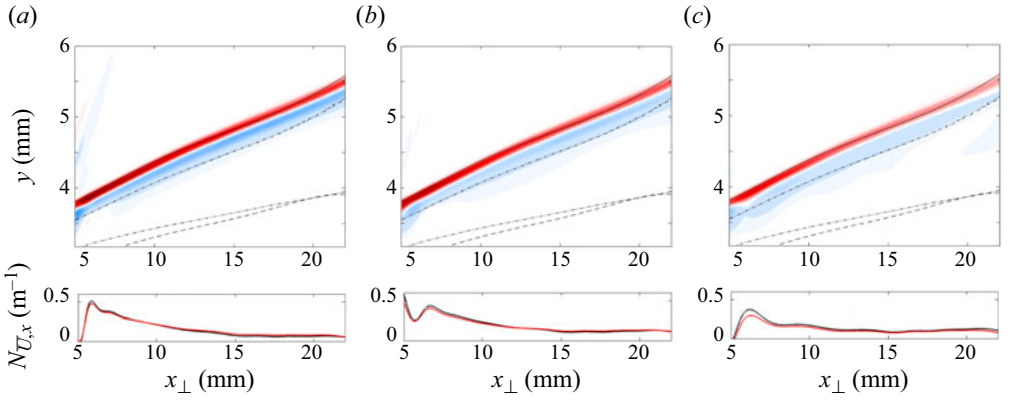

Figure 13. Local growth rate, $\partial N_{\overline{U}}/\partial x$ ($N_{\overline{U},x}$ in label). The colour contour shows the quantity in (4.2) prior to integrating in y. Red and blue colours indicate positive and negative contributions, respectively. Lines mark the boundary-layer edge (solid), reversed flow (dotted) and $\overline{W}_{cf,y} = 0$ (dash-dotted). The line plot is the local growth rate after integrating the contour field (black), and the reconstructed growth rate (red). Panels show (*a*) $\lambda_\parallel = 3.5$ mm, (*b*) $\lambda_\parallel = 5$ mm and (*c*) $\lambda_\parallel = 10$ mm.

energy norm) and contributions from the spatial change in the base flow

$$\frac{\partial N_{\overline{U}}}{\partial x} = \frac{1/2}{\int \tilde{\boldsymbol{q}}^H (\overline{U}_\perp \overline{\boldsymbol{C}}) \tilde{\boldsymbol{q}} \,\mathrm{d}y} \int \left(\underbrace{2\tilde{\boldsymbol{q}}^H \overline{U}_\perp \overline{\boldsymbol{C}} \frac{\partial \tilde{\boldsymbol{q}}}{\partial x}}_{\textit{Budget terms}} + \underbrace{\tilde{\boldsymbol{q}}^H \frac{\partial (\overline{U}_\perp \overline{C})}{\partial x} \tilde{\boldsymbol{q}}}_{\textit{Base-flow terms}} \right) \mathrm{d}y. \tag{4.2}$$

The terms labelled as 'budget terms' in the above equation can be formed independently from each conservation equation. To do this, each equation is multiplied by the complex conjugate of the corresponding primitive variable, and base-flow variables are premultiplied in the equations as needed to match the necessary Chu-energy-norm terms. The budget terms are found in the advection terms on the left-hand side of all equations. All other terms are moved to the right-hand side. Finally, the budget terms in the growth-rate equations are replaced by their corresponding conservation equation, resulting in an expression that can be used to isolate the contribution of individual terms to the growth rate. Additional details on the derivation are given in Appendix B.

4.1. *Dominant productive and destructive terms*

First, the spatial distribution of the growth rate, $\partial N_{\overline{U}}/\partial x$, is examined. The colour contours in figure 13 show the integrand of (4.2), and highlight the main regions where energy is produced (red) or destroyed (blue). All colour contours across the different panels are shown on the same scale. In order to produce a net positive growth rate in the streamwise direction at a given $x_\perp$-position, the y-integral over the red contours beats the y-integral over the blue ones. As the wavelength is increased, we observe that the production and destruction decrease in magnitude. After integrating in y, however, this trend largely disappears and we see that the growth rate has similar magnitudes for the various wavelengths. The 5 mm case appears to be the most-amplified case due to a sustained growth for $x_\perp > 15$ mm and a large production around $x_\perp = 5$ mm.

Important individual terms may now be identified. Terms on the right-hand side of the growth-rate equation (including the base-flow terms) are constructed and probed for their

maximum value. The top ∼25–30 terms are added together in an attempt to reproduce the trends seen in the growth rate. Next, these top terms are grouped based on their tendency to produce or destroy energy, as well as based on the associated physical process (e.g. advection, dissipation, etc.). This helps further eliminate terms with no bearing on the overall trends; for example, terms that make up the pressure-work contribution could be large individually, but when summed, the terms had no contribution to the perturbation energy (by design of the Chu norm) – their character is rather to redistribute energy across the velocity components.

After reducing the list of terms, the growth rate appears to be well represented by only 14 terms from the equations, plus the base-flow contribution. The reconstructed $\partial N_{\overline{U}}/\partial x$ is shown in red in the line plots in figure 13. The retained productive terms consist of generalized Reynolds-stress terms (R_u), Reynolds-heat-flux terms (R_T) and mass-flux terms (R_ρ). The destructive terms consist of dissipation terms (D_u from x-momentum and D_T from the energy equation). The terms are

$$R_u = -\overline{U}_{s,x}\tilde{u}_s^*(\tilde{\rho}\overline{U}_\perp + \overline{\rho}\tilde{u}) - \overline{U}_{s,y}\tilde{u}_s^*(\tilde{\rho}\overline{V} + \overline{\rho}\tilde{v}), \tag{4.3}$$

$$R_T = -c_v\overline{T}_x\frac{\tilde{T}^*}{Ec\,\overline{T}}(\tilde{\rho}\overline{U}_\perp + \overline{\rho}\tilde{u}) - c_v\overline{T}_y\frac{\tilde{T}^*}{Ec\,\overline{T}}(\tilde{\rho}\overline{V} + \overline{\rho}\tilde{v}), \tag{4.4}$$

$$R_\rho = -\frac{\overline{T}}{\overline{\rho}\gamma M^2}\overline{\rho}_y\tilde{v}\tilde{\rho}^*, \tag{4.5}$$

$$D_u = \frac{\mu}{Re}(\tilde{u}_{s,yy} + \tilde{u}_{s,xx})\tilde{u}_s^*, \tag{4.6}$$

$$D_T = \frac{1}{Ec\,Pr\,Re}\frac{\tilde{T}^*}{\overline{T}}(\kappa\tilde{T}_{xx} + \kappa\tilde{T}_{yy} + 2\kappa_T\overline{T}_y\tilde{T}_y), \tag{4.7}$$

where Ec is the Eckert number. The subscripts x or y indicate a derivative with respect to the $x_\perp$ or y directions. Recall the subscript $\perp$ on the base-flow terms indicates components that are aligned with the stability frame, perpendicular to the leading edge (i.e. $\overline{U}_\perp$ is the base-flow velocity in the direction perpendicular to the leading edge of the fin). Some terms, denoted with a subscript s or cf, have been rotated a second time to point in the inviscid streamline direction, ϕ. Velocity terms are only rotated when a grouping allows the rotation to be made without leaving behind factors of ϕ. For example

$$\underbrace{\overline{U}_\perp\tilde{u}}_{x\text{-}mom} + \underbrace{\overline{W}_\perp\tilde{w}}_{z\text{-}mom} = \overline{U}_s\tilde{u}_s + \overline{W}_{cf}\tilde{w}_{cf}. \tag{4.8}$$

This rotation will allow further interpretation on the physical processes at work.

The individual contribution of the productive and destructive terms is shown in figure 14. First, the Reynolds-flux terms are examined. The most productive terms are the $\tilde{\rho}\overline{U}_\perp$ terms (solid lines in the top row of panels), which are attached to x-derivatives of the base flow. For all wavelengths, these are large near the leading edge, dip down, then become large again near the downstream end of the domain. This highlights the importance of the x-derivatives. The $\tilde{\rho}\overline{V}$ contributions from both R_u and R_T (dashed blue and red lines) are negative; in fact, they closely resemble the $\tilde{\rho}\overline{U}_\perp$ contribution for R_u and R_T, but with opposite signs. With the density-fluctuation terms approximately cancelled out, the remaining leading terms are the $\overline{\rho}\tilde{v}$ terms associated with the wall-normal derivatives of base-flow quantities (specifically, $\overline{U}_{s,y}$, $\overline{T}_y$ and $\overline{\rho}_y$). The shape of these terms closely resembles the trends seen in the line graphs of $\partial N_{\overline{U}}/\partial x$ shown in figure 13. The peak in production near the leading edge is captured, along with the reduced production

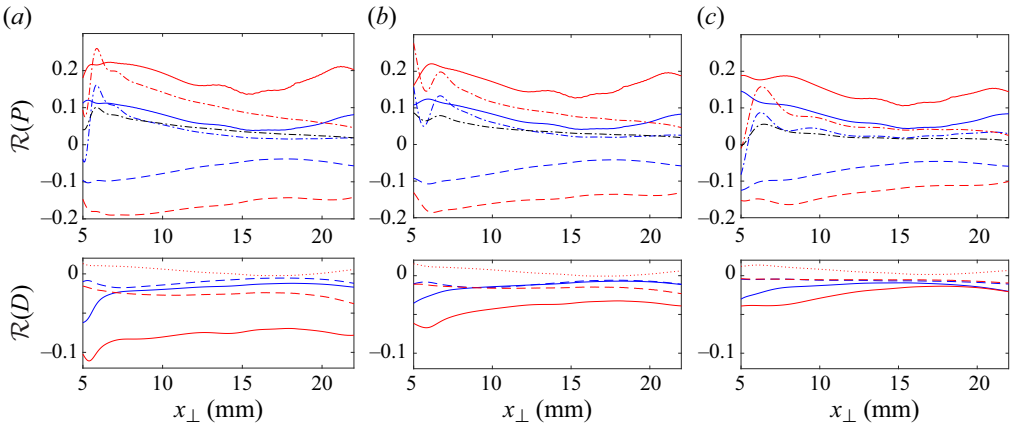

Figure 14. The real part ($\mathcal{R}$) of productive (top row) and destructive (bottom row) terms from the energy budgets. Terms are shown from the x-momentum (blue), energy (red) and continuity (black) equations. Line styles are matched between similar terms. The production terms include: $\tilde{\rho}\overline{U}_\perp$ (solid), $\tilde{\rho}\overline{V}$ (dashed) and $\overline{\rho}\tilde{v}$ (dash-dotted) ($\overline{\rho}_y\tilde{v}$ for the contribution from R_ρ). The destructive terms include: $\tilde{u}_{yy}$ and $\tilde{T}_{yy}$ (solid), $\tilde{u}_{xx}$ and $\tilde{T}_{xx}$ (dashed) and $\overline{T}_y\tilde{T}_y$ (dotted). Panels show (*a*) $\lambda_\parallel = 3.5$ mm, (*b*) $\lambda_\parallel = 5$ mm and (*c*) $\lambda_\parallel = 10$ mm.

for large wavelengths. These results indicate that, despite not being the largest single contributor, the wall-normal derivatives dictate the trends that lead to singling out the 5 mm wavelength as the most-amplified disturbance. It was brought to our attention by a reviewer that the inflection point in the streamwise velocity component lies close to the inflection point in the cross-flow velocity component; thereby, the cross-flow inflection point may control the amplification indirectly.

The dissipation terms are examined next, which are usually destructive. The observation from figure 13 on the weaker dissipative forces for larger-wavelength disturbances is quantified in figure 14, with a large reduction observed in terms associated with y-derivatives. This is expected as the smaller scales associated with the small wavelengths would induce more dissipation. For the 3.5 and 5 mm cases, the x-derivatives appear to make a substantial contribution downstream where their magnitude is nearly equal to the y-derivative terms (particularly, $\tilde{u}_{xx}$ and $\tilde{u}_{yy}$). The heat-flux term, $\overline{T}_y\tilde{T}_y$, is smaller but still necessary to include when reconstructing the spatial-growth rate. However, it does not appear to provide additional insight into the observed trends.

Taken together, figures 13 and 14 demonstrate that the 5 mm wavelength is the most amplified because of a complex balance struck between the productive and destructive terms. The small wavelengths have a larger productive push from the Reynolds-flux terms, but this is outperformed by the destruction stemming from the heat conduction and dissipation terms. Therefore, the small wavelengths experience a smaller amplification. While the destructive terms for the large wavelengths have smaller magnitudes, there is not enough production to result in significant accumulated growth, particularly upstream near the leading edge. This region appears to provide the largest contribution to the integrated N-factor.

Returning to the production terms, the spatial distribution of the terms is examined to understand what terms control the propagation of the perturbation deeper into the boundary layer. Figure 15 shows the two terms responsible: $\overline{\rho}\tilde{u}_s^*(\overline{U}_{s,x}\tilde{u} + \overline{U}_{s,y}\tilde{v})$. The $\overline{\rho}\tilde{v}$ terms were previously identified as the determining factor for the most-amplified wavelength, while $\overline{\rho}\tilde{u}$ had little to no influence on the trends in $\partial N_{\overline{U}}/\partial x$, merely the

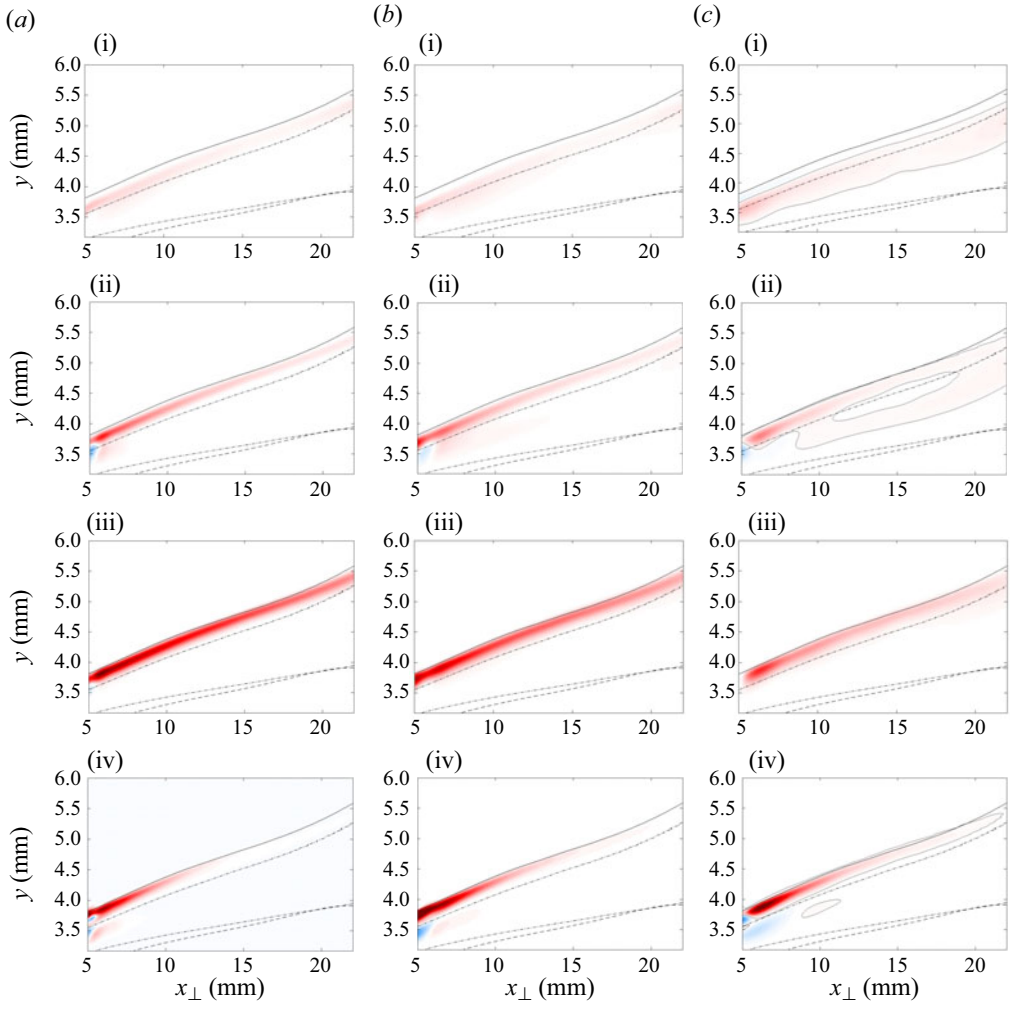

Figure 15. The real part of (i) $\overline{\rho}\tilde{u}^*\overline{U}_{s,x}\tilde{u}$ and (ii) $\overline{\rho}\tilde{u}^*\overline{U}_{s,y}\tilde{v}$, responsible for the stretching of the larger perturbations across the boundary-layer height. The real part of (iii) $-c_v\overline{\rho}(\tilde{T}^*Ec\,\overline{T})(\overline{T}_x\tilde{u}+\overline{T}_y\tilde{v})$, largely confined to the shear layer. The real part of (iv) $-\overline{\rho}\overline{W}_{cf,y}\tilde{v}\tilde{w}^*_{cf}$, magnified 20× in amplitude to make visible. In panels (i-*c*), (ii-*c*) and (iv-*c*), a grey line is overlaid on the lowest positive colour contour to improve visibility. In each plot, lines mark the boundary-layer edge (solid), reversed flow (dotted) and $\overline{W}_{cf,y}=0$ (dash-dotted). Panels show (*a*) $\lambda_\parallel=3.5$ mm, (*b*) $\lambda_\parallel=5$ mm and (*c*) $\lambda_\parallel=10$ mm.

magnitude. However, both terms contribute to the disturbance propagating close to the wall for large wavelengths. Figures 15(i-*c*) and 15(ii-*c*) shown the slightly different spreading behaviour of each term. The value of $\overline{U}_{s,x}\tilde{u}$ shifts lower in the boundary layer, i.e. below the dash-dotted line representing the lower bound of the shear layer in figure 15 and $\overline{U}_{s,y}\tilde{v}$ develops two bands, one remaining in the shear layer and the other developing below the shear layer. Interestingly, the 'twin' terms from R_T (figure 15, row iii) do not contribute to the spreading behaviour. The signature for those terms stays confined to the narrow shear layer.

It should be noted that in the above analysis, no significant contribution from any cross-flow-related term appeared. The peak production from the dominant Reynolds-flux

terms does occur near the leading edge, where base-flow profiles depict typical cross-flow profiles. However, the identified terms are associated with gradients of the streamwise velocity $\overline{U}_s$ (and temperature gradients). This suggests that, while a large cross-flow velocity, and the associated generalized inflection points, may be necessary for instability to occur, they themselves do not produce significant perturbation energy. This is in agreement with a similar energy-budget analysis, performed using LPSE calculations, for the cross-flow instability on a hypersonic yawed cone (Patel *et al.* 2022). The authors indicate that the contribution from the Reynolds stress energy production term related to the wall-normal gradient of the cross-flow velocity is very small compared with the terms that dominantly drive the growth rate, i.e. the Reynolds-heat-flux energy production term and the Reynolds-stress energy production term related to the wall-normal gradient of the streamwise velocity.

Despite their small amplitude, the behaviour of one cross-flow term is examined to support claims made in the discussion on perturbation classification regarding the disturbance growth (or lack thereof) while S-shaped cross-flow base-flow profiles are developing due to the pressure gradient changeover from favourable to adverse. The term examined is

$$R_w = -\overline{\rho}\overline{W}_{cf,y}\tilde{v}\tilde{w}^*_{cf}, \tag{4.9}$$

shown in figure 15 (row iv) with the amplitude magnified 20x to make the colour contours visible compared with the other, more dominant, production terms. This term, containing the wall-normal derivative of the base-flow cross-flow profile, is used to study the production of disturbance energy in the different cross-flow lobes. The dash-dotted line (where $\overline{W}_{cf,y} = 0$) represents each cross-flow maximum in the S-shaped profile. The majority of energy production comes from above the maximum in cross-flow velocity in the first cross-flow maximum that appears (that moves away from the wall as the flow moves downstream). The production decreases for all wavelengths as the flow moves downstream, which we might expect from cross-flow gradient reduction (visible in the base-flow profiles shown in figure 12). Below the upper cross-flow velocity maximum, there is a slight energy contribution where the sign depends on the disturbance wavelength. For smaller wavelengths, R_w tends to be mostly productive in this region, then quickly dies out. This is in line with the expected behaviour of cross-flow disturbances in the presence of a changeover in pressure gradient. However, the location of this changeover in production still lies within the first cross-flow lobe, not the secondary one near the wall as expected. (Note that, for all wavelengths, there is no visible energy contribution from the lower cross-flow lobe.) Additionally, R_w for the large wavelength is destructive in this region, then becomes very slightly productive (the lower productive contour level is outlined in grey to improve visibility). This behaviour is opposite that expected for the cross-flow-like disturbances, and further demonstrates a distinct behaviour for the large-wavelength disturbances.

4.2. *Wall heat-flux analysis*

The above analysis provides some understanding on why large-wavelength disturbances spread from the shear layer deeper towards the wall. However, it is difficult to apply this insight directly to the N_{q_w} amplification measurement, as that stems from the behaviour of $\partial\tilde{T}/\partial y$ at the wall. To better understand the trends in N_{q_w}, the energy equation is taken and evaluated at the wall. Wall boundary conditions (Dirichlet zero on all terms except

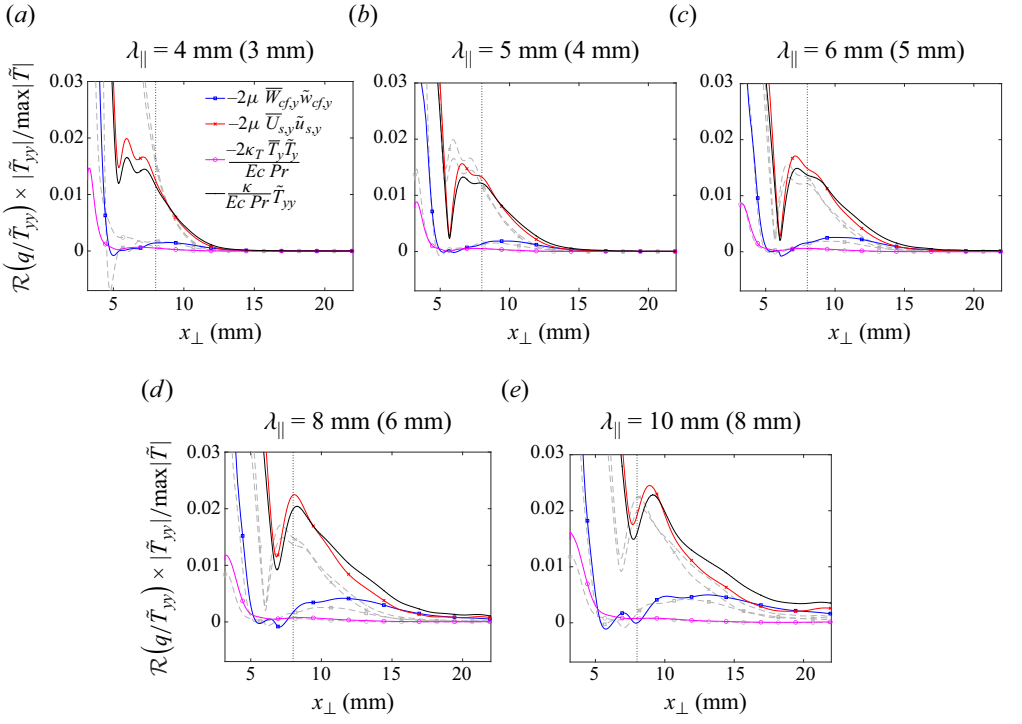

Figure 16. Contributors to the wall heat flux (black line) as derived from the energy equation evaluated at the wall for stationary perturbations at $Re' = 11 \times 10^6$ m^{-1}. Each panel represents two wavelengths. The primary wavelength uses coloured lines and the secondary wavelength uses dashed grey lines and is listed in parenthesis. The vertical dotted line marks the start of the reversed-flow region.

$\overline{\rho}$ and $\tilde{\rho}$, and isothermal on $\overline{T}$) reduce the energy equation down to five terms, which are rearranged to solve for $\tilde{T}_{yy}$ as a proxy for the heat flux

$$\frac{\kappa}{Ec\ Pr}\tilde{T}_{yy} = -2\mu\overline{U}_{s,y}\tilde{u}_{s,y} - \frac{8}{3}\mu\overline{V}_y\tilde{v}_y - 2\mu\overline{W}_{s,y}\tilde{w}_{s,y} - \frac{2\kappa_{\overline{T}}}{Ec\ Pr}\overline{T}_y\tilde{T}_y. \tag{4.10}$$

The velocity terms have again been rotated to align with the inviscid streamline.

The magnitude of the individual terms is shown in figure 16. The quantities are normalized to isolate the size of the wall heat flux relative to the amplitude of $\tilde{T}$ and enable a comparison between wavelengths. The contribution from $\overline{V}_y\tilde{v}_y$ and $\overline{T}_y\tilde{T}_y$ is negligible and therefore omitted from the plots. The value of $\tilde{T}_{yy}$ is large near the leading edge, and decays further downstream, mirroring the behaviour seen in N_{q_w}. For the large wavelengths, $\tilde{T}_{yy}$ does not decay to zero near the end of the domain, instead remaining finite and nearly constant for the last 5 mm. For all wavelengths, the frictional heating term associated with the streamwise velocity $\overline{U}_s$ dominates the behaviour of $\tilde{T}_{yy}$ near the leading edge. This is in line with what was observed in the total-energy analysis – the wall-normal derivatives of the streamwise velocity dominate the amplification behaviour. For the smallest wavelengths, there is a slight contribution from the cross-flow term in the range $x_\perp = 7$–10 mm, but it quickly diminishes downstream. As the wavelength increases, the $\overline{W}_{cf,y}\tilde{w}_{cf,y}$ term becomes more significant and sustained downstream. This reflects the increased presence of the disturbance within the reversed-flow region for large wavelengths.

It is interesting that a near-wall analysis does reveal an important contribution (in some large-wavelength cases) from cross-flow-related terms, in contrast to the total-energy-budget analysis that examined the entire flow. It is important to note that comparing the cross-flow effect at the wall and far away from the wall necessitates regarding different terms, i.e. the viscous heating term ($2\mu\overline{W}_{cf,y}\tilde{w}_{cf,y}$) and the advection-driven Reynolds-stress term ($\overline{\rho}\tilde{w}^*_{cf}\tilde{v}\overline{W}_{cf,y}$), respectively. Therefore, the influence of cross-flow has a different nature and cannot be directly compared.

Nevertheless, we suspect that viscous effects near the wall remove a dominant flow direction in the reversed-flow region, whereas the free-stream (and therefore streamwise) flow-advection effects dominate the shear layer. Accordingly, we expect the cross-flow velocity component to support a large wall-normal gradient near the wall as compared with the shear layer. This is supported by figure 12, which shows that that $\overline{W}_{cf,y}$ decays in the neighbourhood of the shear layer for $x_\perp = 8$ mm, while maintaining its magnitude near the wall.

5. Effect of free-stream unit Reynolds number

The free-stream unit Reynolds number is now increased to $Re' = 22 \times 10^6$ m^{-1}. At these free-stream conditions, experiments performed in the Air Force Academy Mach 6 Ludwieg Tube documented thermal striations on the fin surface indicative of transition to turbulence (Middlebrooks *et al.* 2022). The present laminar simulations indicate the overall base-flow structure remains the same. However, the boundary-layer thickness shrinks as expected due to the increased Reynolds number, and the stationary vortices in the laminar base flow develop additional rollovers. In the stability frame of reference, the reversed-flow region persists and moves slightly in the streamwise direction. It begins at $x_\perp = 6$ mm, slightly farther upstream compared with the reversed flow in the lower-Reynolds-number case which began at 8 mm.

5.1. *Comparison with experiment*

In the experimental results for $Re' = 22 \times 10^6$ m^{-1}, transition is observed between 10 and 15 mm from the leading edge. This implies the presence of nonlinear effects and this should be accounted for at least downstream of $x_\perp = 10$ mm when attempting to compare our data. At 3 mm from the leading edge, the experimental wavelet analysis shows a response in the range of 1.5–5 mm spanwise wavelength. At 8 mm, those wavelengths are still active, but a dominant band from 10 to 12 mm spanwise wavelength is now present (Middlebrooks *et al.* 2022).

The N-factors, as calculated for stationary disturbances, are shown in figure 17. According to the Chu-energy definition the most-amplified wavelength decreases to 3.5 mm at this Reynolds number. Additionally, the majority of the stationary disturbances are more amplified compared with the lower-Reynolds-number case, as the most-amplified wavelength reaches an N of 4.75 by $x_\perp = 22$ mm ($N_{E,max} = 3.47$ for stationary perturbations at $Re' = 11 \times 10^6$ m^{-1}). The large wavelengths do not show a large change in amplification. N_E for the 10 mm wave, for example, only increases from 2.4 to 2.7 at $x_\perp = 22$ mm. An alternative amplification measurement, again based on surface heat flux, continues to show a bias towards larger wavelengths. In this case, the 10 mm wave becomes more amplified than the 7 mm wave around $x_\perp = 15$ mm downstream; the 3.5 mm wave is never the most-amplified disturbance according to this measurement.

We believe the smaller wavelengths present in experimental results are in agreement with the smaller wavelengths predicted by our HLNS analysis at $Re' = 22 \times 10^6$ m^{-1}.

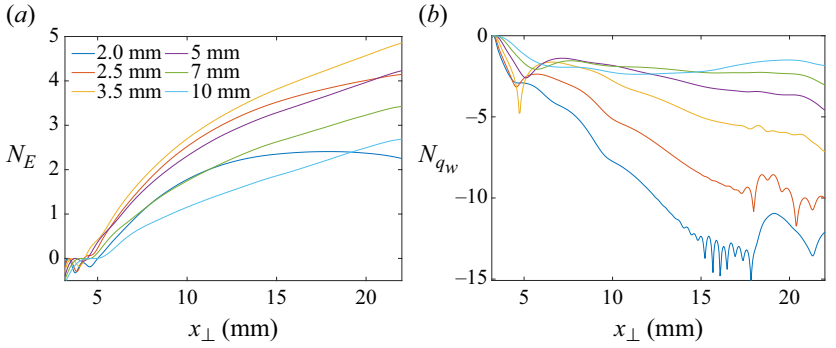

Figure 17. The N-factors for stationary disturbances at $Re' = 22 \times 10^6$ m^{-1} based on Chu energy (a) and surface heat flux (b).

The theoretical prediction due to HLNS indicates that 3.5 mm is the most-amplified wavelength from $x_\perp = 5$ mm onward according to the Chu-energy norm. This fits with the range of 1.5–5 mm reported by experiments measured at $x_\perp = 3$ and 8 mm. The experimental results at $Re' = 22 \times 10^6$ m^{-1} indicate that 10–12 mm wavelengths are the most dominant instability when transition occurs (around 10–15 mm downstream of the leading edge). Our N-factor results according to the Chu-energy norm do indicate that the 10 mm wavelength is unstable. However, it is not close to being most amplified. When we switch our metric to a wall-based measurement (N-factor according to heat flux) to better match experimental methods, our results indicate that larger wavelengths are in fact more dominant closer to the wall, consistent with what the experiment would measure. The specific 10 mm wavelength is more dominant compared with smaller wavelengths in this metric, however, it does not become the most-amplified wavelength until $x_\perp = 15$ mm, which is downstream of the transition location measured in experiments. The actual wavelengths observed in experiments could be a result of receptivity or nonlinear effects not accounted for in the present linear analysis. However, the switchover from smaller wavelengths dominant upstream to larger wavelengths measured at the wall downstream we believe is captured by our linear results demonstrating how smaller wavelengths are lifted further from the wall by the shear layer.

Turning to the HLNS N-factor calculations for unsteady disturbances, similar trends are observed as for the stationary disturbances and are shown in figure 18. Overall, the disturbances are more amplified at this higher Reynolds number. The band of disturbances with $N > 6$ stretches between 3 and 5 mm and 90 to 150 kHz, with smaller wavelengths becoming more amplified at higher frequencies compared with the $Re' = 11 \times 10^6$ m^{-1} case. The most-amplified disturbance based on the Chu-energy norm (shown in figure 18a) is $\lambda_\parallel = 3.5$ mm at 110 kHz. This wave reaches a maximum N-factor of 6.54, which is larger than the maximum N-factor of 4.99 for the previously most-amplified wave (5 mm, 75 kHz) at $Re' = 11 \times 10^6$ m^{-1}. These measurements are again compared with amplification factors computed based on wall-pressure signatures, shown in figure 18(b). With this definition, the most-amplified disturbance band shifts to larger wavelengths and lower frequencies. A broad band of 'most-amplified' wavelengths is present in this measurement compared with the Chu-energy results. Disturbances between 4.5 mm ($\sim$85 kHz) and 11 mm ($\sim$25 kHz) appear nearly equally amplified according to the wall-pressure amplification measurement. This reinforces how determining the dominant waves becomes challenging when only using information at the wall.

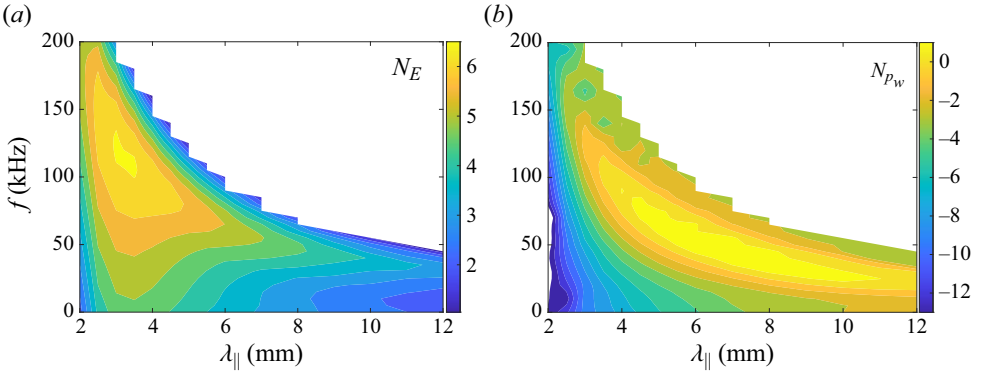

Figure 18. The N-factors for travelling disturbances at $Re' = 22 \times 10^6$ m^{-1} based on Chu energy (a) and surface pressure (b). Measurements made at $x_\perp = 22$ mm.

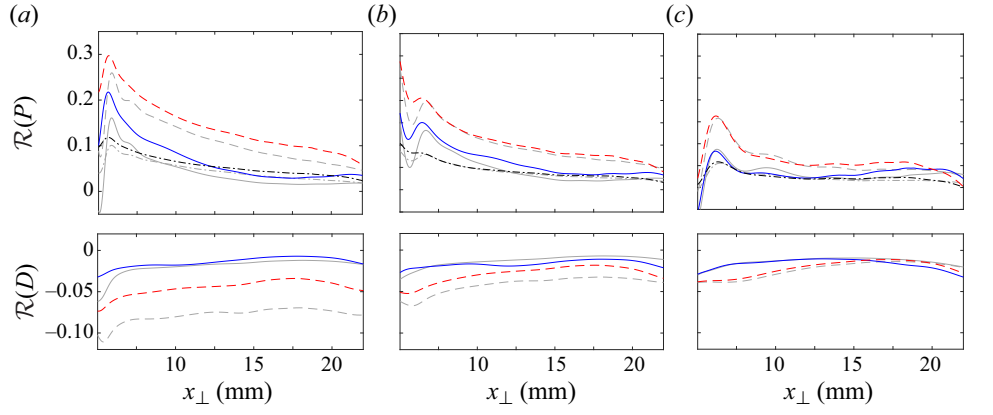

Figure 19. Comparing the real part of the main productive (top row, $\bar{\rho}\tilde{v}$) and destructive (bottom row, $\tilde{u}_{yy}$ and $\tilde{T}_{yy}$) terms from the energy budgets between $Re' = 22 \times 10^6$ m^{-1} (coloured lines) and $Re' = 11 \times 10^6$ m^{-1} (grey lines). Terms from the x-momentum (blue), energy (red) and continuity (black) equations are shown. Grey lines use the same line style of the matching coloured line to identify particular terms. Panels show (a) $\lambda_\parallel = 3.5$ mm, (b) $\lambda_\parallel = 5$ mm and (c) $\lambda_\parallel = 10$ mm.

5.2. *Energy analysis: wavelength selection*

The Chu-energy-budget analysis is repeated for this case. We find the same terms are dominant as for $Re' = 11 \times 10^6$ m^{-1}, therefore we focus on how the dominant terms change for the $Re' = 22 \times 10^6$ m^{-1} case. The main productive and destructive terms (the wall-normal Reynolds-flux and dissipation terms) are shown in figure 19 and compared between the two Reynolds numbers. First, the 3.5 mm case is examined to understand how it overtakes the 5 mm case as most amplified. All three productive terms show an increased contribution to the growth rate across the streamwise domain. However, in the 5 mm case, only the region near the leading edge features an increase in production in all the terms examined. Comparing the destructive terms, the 3.5 and 5 mm cases both have decreased destruction due to the $\tilde{T}_{yy}$ term. In the 3.5 mm case, the $\tilde{T}_{yy}$ destruction at $Re' = 22 \times 10^6$ m^{-1} is nearly half that corresponding to the lower Reynolds number.

The large decrease in destruction for the 3.5 mm wave is somewhat counterintuitive. The increase in Reynolds number leads to a thinner boundary layer, so it is natural to expect the smaller scales would lead to an increase in dissipation. To understand these results,

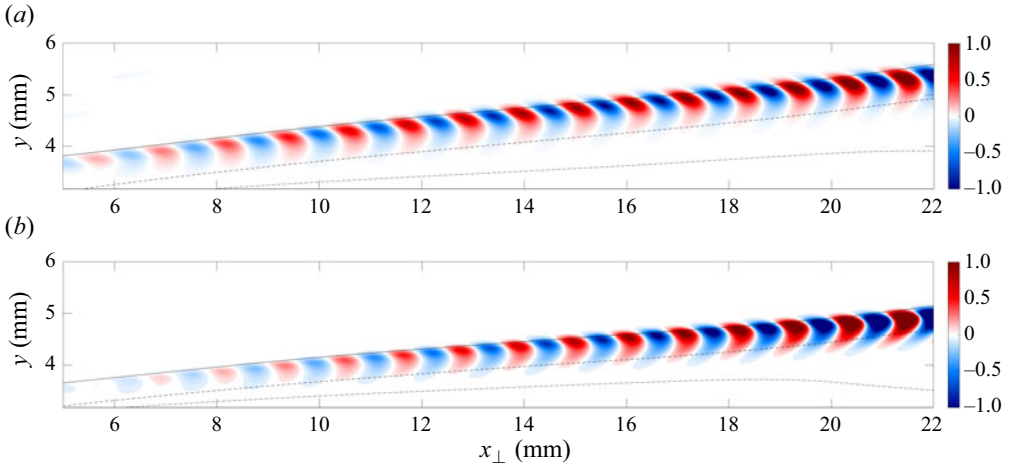

Figure 20. Disturbance ($f = 0$ kHz, $\lambda_{\parallel} = 3.5$ mm) visualized using $\mathcal{R}(\tilde{T})/\max|\tilde{T}|$ scaled to 1 near $x_{\perp} = 16$ mm. Lines mark the boundary-layer edge (solid), reversed flow (dash-dotted) and $\overline{W}_{cf} = 0$ (dashed). Panels show (*a*) $Re' = 11 \times 10^6$ m^{-1} and (*b*) $Re' = 22 \times 10^6$ m^{-1}.

the 3.5 mm wave is shown in figure 20 using $\mathcal{R}(\tilde{T})$ scaled to 1 around $x_{\perp} = 16$ (so to better visualize the following discussion). This figure demonstrates the perturbation does not behave in a self-similar way as the Reynolds number increases. Rather, the 3.5 mm wave redistributes (vertically stretches) to better fit the shear layer that exists between the boundary-layer edge and $\overline{W}_{cf} = 0$. The stretched disturbance signature leads to the decrease in $\tilde{T}_{yy}$.

For the lower-Reynolds-number case, an optimum balance between productive and destructive terms determined the selection of the most-amplified wavelength. Wavelengths smaller than the one that is most-amplified were shown to have high production, but also large destruction which prevented the overall amplification of small wavelengths from being competitive. At this higher Reynolds number (and, correspondingly, within the thinner boundary layer) the relevant scales have become smaller and therefore can support the smaller wavelengths. Besides the slight increase of production terms, this is primarily attributed to the destructive terms no longer overwhelming the production for the 3.5 mm case. Consequently, the N-factor increases enough to become the most-amplified wavelength. Conversely, only slight changes are present in the 10 mm wavelength production and destruction. The change in length scales caused by the increased Reynolds number is insignificant compared with the large-wavelength scale, rendering the 10 mm wave nearly unaffected by the Reynolds-number change.

6. Sensitivity to yaw

Thus far, all fin-cone studies have been restricted to a zero-degree angle of attack and yaw. The effect of small yaw angles is relevant when considering off-nominal cases in flight experiments, as well as possible sources for disagreement between experiments and companion computations. There are multiple sources for uncertainty in yaw; control adjustments during flight could cause small yaw angles, and possible contributors in experiments include the physical set-up of the model and possible flow angularity in wind tunnels. The limits on the yaw angles studied here were informed by reports on flow angularity in various supersonic wind tunnels, which tended to range from ± 0.2

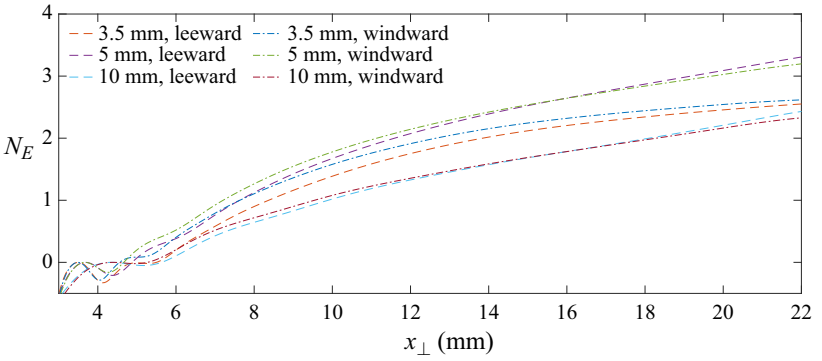

Figure 21. Change in Chu-energy amplification due to small yaw angles. Included in the plot are calculations from the nominal case (solid lines), leeward side (dashed) and windward side (dash-dotted). Simulations use $Re' = 11 \times 10^6$ m^{-1}.

to 0.5° (e.g. Jackson, Corlett & Monta 1981; Vallabh & Skews 2017). For this reason, one fully three-dimensional simulation is conducted with 0.5° yaw introduced for $Re' = 11 \times 10^6$ m^{-1}.

Both the windward and leeward sides of the three-dimensional simulation are examined, where the global location of the stability plane relative to the model is the same as the zero-incidence cases. Steady wall forcing is applied and the effect of yaw on stationary disturbances is quantified. The results are shown in figure 21. There are only small changes in the overall amplification of the disturbances, i.e. the perturbations are relatively insensitive to the small yaw angles applied. The most-amplified wavelength does not change within the chosen wavelength sampling (0.25 mm steps in $\lambda_\parallel$). The dominant effect near the leading edge is a streamwise shift in the N-factors which is more pronounced for smaller wavelengths.

The wall-normal Reynolds-flux terms, previously shown to match the trends in the growth rate, are examined near the leading edge in figure 22. Again, the dominant effect is an apparent shift in where the major energy production occurs. On the windward side, the wall-normal term is activated further upstream compared with the leeward side. This is in agreement with trends observed in prominent base-flow features, e.g. the reversed-flow region begins approximately 0.6 mm further upstream in the windward case ($x_\perp = 7.7$ mm vs 8.3 mm in the leeward case).

The base-flow profiles corresponding to the region examined in the energy analysis are shown in figure 23. The cross-flow profiles are interesting because the leeward side is seen to have a slightly larger cross-flow velocity near the leading edge. This suggests the leeward side should support a stronger cross-flow instability, as the cross-flow instability has been shown to correlate with $\overline{W}_{cf}$ (or M_{cf}, as in Chen *et al.* 2022*b*). However, the shifts shown in the energy budget and the movement of the reversed-flow region suggest that it is more appropriate in this case to view the leeward cross-flow profiles as lagging behind the windward profiles in the streamwise direction, rather than being truly larger.

This simulation yields insight beyond the effect on fin leading-edge instabilities by providing the first quantification of yaw effects on base-flow behaviour over the entire finned cone. Two key areas are shown in figure 24, where the original Mach contour lines from the zero-degree yaw case are overlaid on the yawed simulation colour contours. The flow on the fin near the leading edge is not visibly affected by the yaw. This agrees with the previous results showing only small changes in the N-factor. Some movement in the

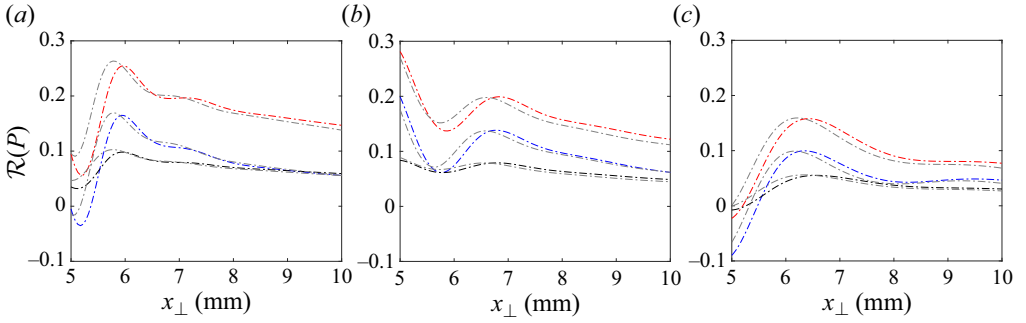

Figure 22. Comparing the real part of the dominant productive terms from the energy budgets between the leeward side (coloured lines) and the windward side (grey lines). The blue, red and black lines correspond to terms taken from x-momentum, and energy and continuity equations, respectively. Panels show (*a*) $\lambda_\parallel =$ 3.5 mm, (*b*) $\lambda_\parallel = 5$ mm and (*c*) $\lambda_\parallel = 10$ mm.

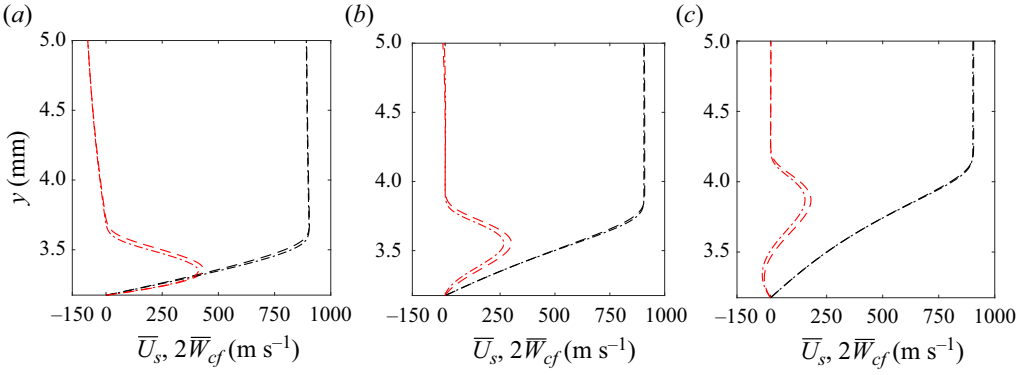

Figure 23. Comparing rotated base-flow profiles near the leading edge between the leeward (dashed) and windward (dash-dotted) sides at $Re' = 11 \times 10^6$ m^{-1}. Shown are the streamwise (black) and cross-flow (red) velocities. The cross-flow velocities are doubled to improve visibility. Panels show (*a*) $x_\perp = 3.5$ mm, (*b*) $x_\perp =$ 5 mm and (*c*) $x_\perp = 8$ mm.

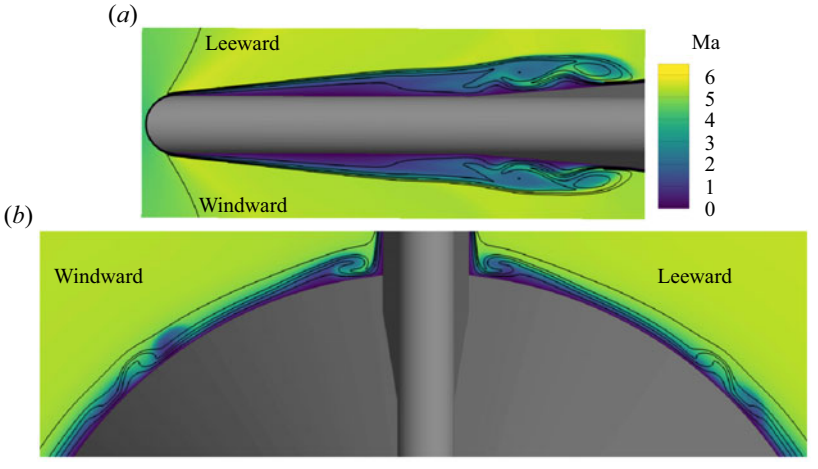

Figure 24. Change in base-flow vortices due to small yaw angles at $X = 0.35$ m. Simulations at $Re' = 11 \times 10^6$ m^{-1}. The zero-degree yaw case is represented by Mach contour lines (black) overlaid on the colour contours of the 0.5° yaw case. Images focus on (*a*) flow on the fin, and (*b*) flow on the cone surface.

fin vortex position is observed; the vortex is located higher on the fin in the windward case compared with the leeward case. The most prominent change is seen in the location of the outboard cone vortex on both sides of the cone. At the streamwise station shown ($X = 0.35$ m), each vortex is shifted a distance nearly equal to the width of the cone vortex ($\sim 7^\circ$). While difficult to quantify, the overall shape of the vortex does not appear to be substantially altered. Further studies should examine the effect, if any, of the yaw angle on perturbation growth inside the cone vortex. These results do suggest that the cone-vortex location is highly sensitive: slight yaw angles will greatly enhance uncertainty in its location.

7. Conclusions

The growth of oblique disturbances on a highly swept fin was examined using HLNS. The flow is assumed to be spanwise infinite, but possible elliptic effects due to reversed flow in the leading-edge-perpendicular frame are accounted for by allowing a general disturbance in the streamwise direction. Wall blowing and suction (both steady and unsteady) applied near the leading edge produced wave-like disturbances which were localized away from the wall. Disturbance amplification, wave angles and phase speeds were quantified. Additionally, a spatial energy-budget analysis was formulated to understand the physical processes determining the most-amplified wavelength and the behaviour of the disturbance structure, particularly near the wall.

One major finding regarding the disturbance behaviour was on how small-wavelength disturbances (including the most-amplified disturbances) tend to remain confined within a narrow region of the boundary layer, correlating with the shear layer between the boundary-layer edge and where the cross-flow velocity $\overline{W}_{cf} = 0$. As the disturbance wavelength increases, the perturbation structure propagates deeper into the boundary layer, including the reversed-flow region. This motivated alternate amplification definitions based on wall quantities, which, when compared with an amplification definition based on total energy, showed a consistent bias towards larger wavelengths and lower frequencies.

The spatial energy budget formulated for HLNS revealed that, despite not being the largest contributor to the perturbation growth, the wall-normal Reynolds-flux terms dictated the growth-rate trends, with those related to heat flux being most dominant. Other large contributors included terms associated with both x- and y-derivatives of the streamwise velocity component. No cross-flow terms had large magnitudes compared with terms associated with the streamwise flow. Additionally, Reynolds-stress terms were identified as controlling the localization of small wavelengths in the shear layer, and large wavelengths throughout the boundary layer. This behaviour directly leads to the bias in amplification based on wall quantities.

Finally, the effect of Reynolds number and small yaw angles was examined. The higher-Reynolds-number case corresponds to experimental conditions that produced transition on the surface of the fin (Middlebrooks *et al.* 2022). The most-amplified wavelength predicted by HLNS (according to the Chu-energy norm) did correspond with measured wavelengths near the leading edge. However, the experimentally measured wavelength at transition was much larger than that predicted by HLNS. However, when also considering amplification based on wall quantities, HLNS calculations do provide at least a partial explanation for the experimentally observed switchover from smaller wavelengths dominant upstream to larger wavelengths measured near transition. The energy analysis revealed that the larger amplification for small wavelengths (compared with the lower-Reynolds-number case) was primarily driven by a decrease in dissipation. In order to reduce wall-normal derivatives, the small-wavelength perturbations

redistributed in the boundary layer, resulting in a structure that overlapped the shear layer more effectively. When considering the effect of yaw, we found that any changes in amplification were slight, indicating that the disturbances are not overly sensitive to small changes in yaw. In fact, the dominant effect was a streamwise shift that resulted in the windward side becoming more amplified farther upstream. The energy analysis in both parameter variations continues to reinforce that the wall-normal Reynolds-flux terms related to the inviscid-streamwise velocity and temperature of the base flow are the major driver of the most-amplified trends, rather than any cross-flow-related terms.

The instability of flow over the fin to wall blowing and suction has been thoroughly examined, and the linear dynamics of the resulting oblique perturbations characterized and analysed through a spatial energy analysis. These results provide a better understanding of the underlying mechanisms driving perturbation growth. This is particularly important given the complex boundary layer that exists on the fin, which calls for general stability analysis tools such as HLNS. Thus far, the perturbation dynamics has only been examined in a linear analysis. While this may be acceptable for the scenarios examined in this paper due to the small N-factors, cases that produce significant amplification would warrant further nonlinear investigations. Additionally, the importance of boundary-layer receptivity to both surface roughness and free-stream noise in disturbance selection and eventual transition scenarios cannot be overlooked, and should be the study of future investigations.

Acknowledgements. The authors are grateful to Pointwise for providing the mesh software and to NASA for providing DPLR. Portions of this research were conducted with the advanced computing resources provided by Texas A&M High Performance Research Computing. The authors also acknowledge the Texas Advanced Computing Center at The University of Texas at Austin for providing HPC and storage resources that have contributed to the research results reported within this paper. The authors would also like to acknowledge the helpful comments provided by reviewers which led to further insights presented in this paper.

Funding. This work is supported by the Office of Naval Research under ONR grants N00014-16-1-2434 and N00014-19-1-2500 with Program Manager Eric Marineau.

Declaration of interests. The authors report no conflict of interest.

Author ORCIDs.
Madeline M. Peck https://orcid.org/0000-0001-8881-9771;
Koen J. Groot https://orcid.org/0000-0001-7383-5525.

Appendix A. Numerical convergence

The HLNS method exhibits a large sensitivity to grid resolution and boundary conditions due to the inherent elliptic nature of the problem. Results from the $Re' = 22 \times 10^6$ m^{-1} solution are examined on three different grids to ensure accuracy in the presented results. The baseline grid has 701 points in the streamwise direction and 586 points in the wall-normal direction. One grid increases the streamwise resolution to 1050 points, and one grid increases the wall-normal resolution to 879 points. All solutions used sixth-order finite-difference stencils and the same buffer parameters.

Convergence of the stability problem vs grid resolution is shown in figure 25. Amplification (assessed via the energy norm (3.1)) is computed for two steady disturbances with spanwise wavelengths of 2 and 12 mm. Results are only shown where no buffer is applied. The results are nearly indistinguishable. The largest error is present in the smallest-wavelength case, where there is a discrepancy of 0.012 units in N_E at $x_\perp =$ 25 mm. Based on these results, the coarse grid resolution is deemed sufficient for this study.

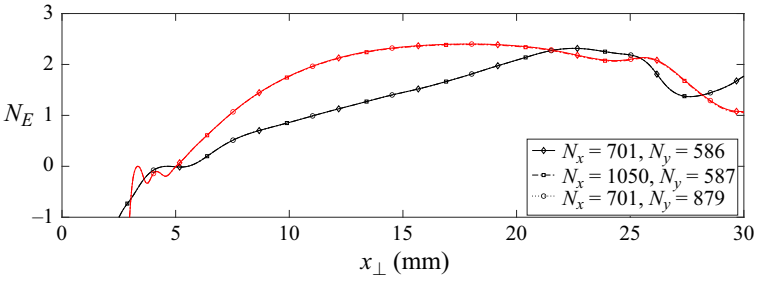

Figure 25. Stability grid convergence results for stationary disturbances at $Re' = 22 \times 10^6$ m^{-1}. The red line is $\lambda_\parallel = 2$ mm, and the black line is $\lambda_\parallel = 10$ mm. The different symbols and line styles represent the different grid resolutions.

Buffer zones are used at the outlet and free stream to damp outgoing waves and prevent non-physical reflections from affecting the results. The buffer function at the outlet is

$$\mathcal{B} = \sigma \left(\sin \left(\frac{\pi}{2} \frac{\xi - \xi_B}{\xi_{max} - \xi_B} \right) \right)^p, \quad \text{for } \xi > \xi_B, \tag{A1}$$

$$\mathcal{B} = 0 \quad \text{otherwise.} \tag{A2}$$

The amplitude σ, power p and location of the buffer ξ_B are variable. In the free stream, the same function is used with η replacing ξ, and a unique η_B, σ and p may be specified. The buffer is added to the equations as

$$(\boldsymbol{M} + \mathcal{B}\boldsymbol{I}^*)\tilde{\boldsymbol{q}} = \boldsymbol{f}, \tag{A3}$$

where $\boldsymbol{I}^*$ is a special identity function distributing the buffer function equally across the components in $\tilde{\boldsymbol{q}}$ in (2.4) within the buffer regions. The buffer does not ever intersect with the region where the forcing function is applied. Numerical experiments shown in this section verified the independence of the presented results to the buffer location and amplitude.

Buffer effects at both the free stream and outlet are examined by comparing disturbance energy across simulations with different buffer parameters. The start of the buffer location is tested at 85 %, 90 % and 95 % of the domain length (and applied until the end of the domain), and the buffer amplitude is varied as 25, 50 and 100. The free-stream buffer has no effect on the disturbance energy. The outlet buffer effects are more complicated and depend on the disturbance wavelength and frequency. For this reason a small parameter sweep is conducted to understand the buffer effect. For the high-Reynolds-number case, $\lambda_\parallel = 3.5$, 5, 8 and 12 mm were studied. The frequencies studied per spanwise wavelength were localized around the frequency with the maximum disturbance energy. Results are presented only for limited frequencies in the $\lambda_\parallel = 3.5$ and 8 mm cases as these are representative of the results seen across the entire parameter study.

Figure 26 shows the effect of the outlet buffer on disturbance energy for the $\lambda_\perp = 3.5$ mm disturbance. As intended, the effects are localized near the outlet. The larger buffer amplitude σ results in a sharper decline in energy when the buffer is activated. Moving the location of the buffer region generally moves the region of decay backwards, however, this becomes more unpredictable as the disturbance frequency becomes large. Figure 26(*c*) shows a case where this is true, as the $x_b = 90$ % case deviates from the behaviour observed for the 85 % and 95 % cases. Still, figure 26 provides confidence in

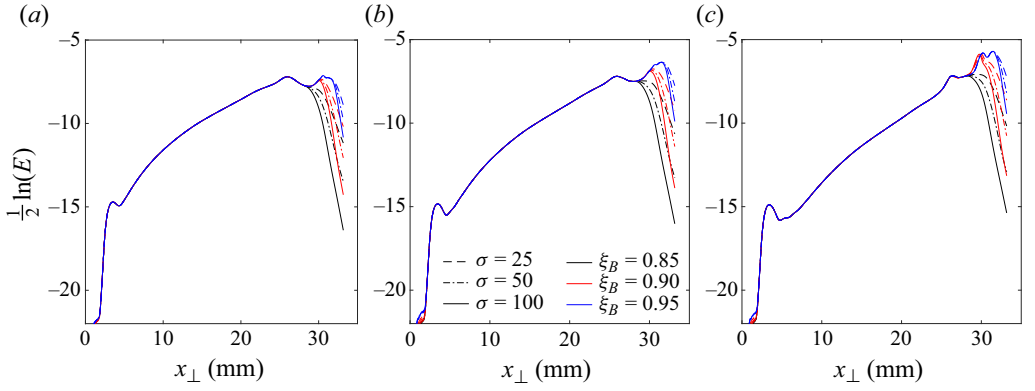

Figure 26. Disturbance energy for $\lambda_\perp = 3.5$ mm with varying buffer parameters. Panels show (*a*) $f = 100$ kHz, (*b*) 120 kHz and (*c*) 140 kHz.

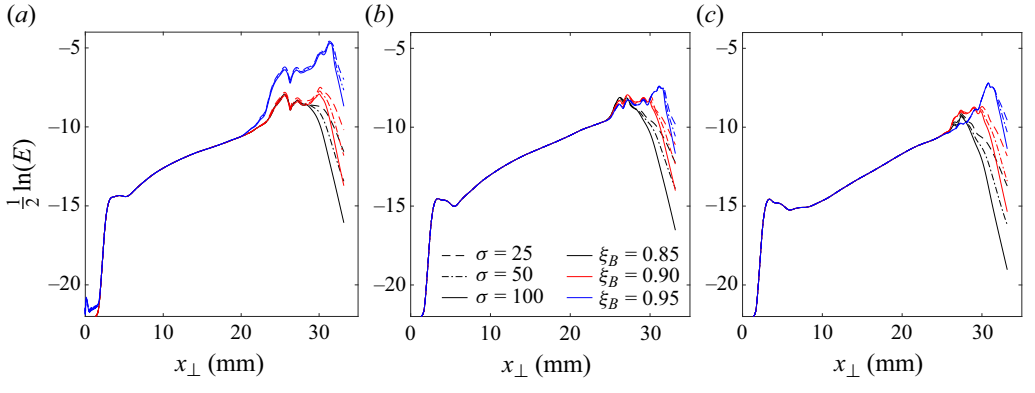

Figure 27. Disturbance energy for $\lambda_\perp = 8$ mm with varying buffer parameters. Panels show (*a*) $f = 40$ kHz, (*b*) 50 kHz and (*c*) 60 kHz.

claiming the buffer effects are largely localized, and unimportant for results examined upstream of $x_\perp = 25$ mm.

Figure 26 indicates that the influence of the buffer propagates further upstream as the disturbance frequency is increased. The frequency where these effects become more important becomes smaller as the disturbance spanwise wavelength is increased. Generally speaking, the peak frequency is captured before the buffer effects become too large to meaningfully measure the disturbance in the domain of interest. Figure 27 provides one counter example where the buffer effects are felt far upstream at a frequency lower than the peak frequency. In figure 27(*a*), when the buffer is applied only after $x_b = 95\,\%$, there is a large change in the measured disturbance energy up to $x_\perp = 20$ mm. There is much better agreement between the $x_b = 85$ and 90 % cases.

After closely examining multiple similar results, the buffer parameters are fixed at $x_b = 90\,\%$ and $\sigma = 50$. Results are also limited $x_\perp = 22$ mm to be certain no buffer effects pollute the presented data. This does not hinder the objective of this paper, as $x_\perp = 23$ mm approximately aligns with where the fin vortex begins for the high Reynolds cases. As we are interested in disturbance evolution much prior to this point, there is no need to take data further down the domain.

Appendix B. Spatial energy-budget formulation

The spatial energy-budget formulation is presented here in more detail. The driving goal is to explain what terms are responsible for the behaviour of the spatial-growth rate, and therefore the N-factor. With this in mind, we begin by expanding the expression for disturbance amplification (4.1)

$$N_{\overline{U}} = \frac{1}{2}\ln\int \overline{U}_\perp \left(\overline{\rho}(|\tilde{u}|^2 + |\tilde{v}|^2 + |\tilde{w}|^2) + \frac{\overline{\rho}}{\gamma(\gamma-1)M^2\overline{T}}|\tilde{T}|^2 + \frac{\overline{T}}{\gamma M^2\overline{\rho}}|\tilde{\rho}|^2\right) \mathrm{d}y. \quad \text{(B1)}$$

We are interested in spatial growth, therefore the x-derivative of this expression is taken (displayed in shortened form in (4.2)). Note that both the base-flow and perturbation variables are functions of space, which results in the 'base-flow terms' appearing in the growth rate (4.2). To make further manipulations clear, here we expand the bracketed 'budget terms' expression

$$\overline{\rho}\overline{U}_\perp\tilde{u}^*\tilde{u}_x + \overline{\rho}\overline{U}_\perp\tilde{v}^*\tilde{v}_x + \overline{\rho}\overline{U}_\perp\tilde{w}^*\tilde{w}_x + \frac{\overline{\rho}\overline{U}_\perp}{\gamma(\gamma-1)M^2\overline{T}}\tilde{T}^*\tilde{T}_x + \underline{\frac{\overline{T}\,\overline{U}_\perp}{\gamma M^2\overline{\rho}}\tilde{\rho}^*\tilde{\rho}_x}. \quad \text{(B2)}$$

A subscript indicates a derivative with respect to the indicated direction, and a star indicates the complex conjugate.

Next, we would like to replace the above terms with the conservation equations to allow examination of individual terms representing specific physical processes. As an example, consider the continuity equation written for HLNS, which reads

$$\begin{aligned}\frac{\mathrm{D}\tilde{\rho}}{\mathrm{D}t} &= -\mathrm{i}\omega\tilde{\rho} + \underline{\tilde{\rho}_x\overline{U}_\perp} + \tilde{\rho}_y\overline{V} + \mathrm{i}\beta\tilde{\rho}\overline{W}_\perp \\ &= -\mathrm{i}\beta\overline{\rho}\tilde{w} - \overline{\rho}\tilde{v}_y - \overline{\rho}_y\tilde{v} - \tilde{\rho}\overline{V}_y - \overline{\rho}\tilde{u}_x - \overline{\rho}_x\tilde{u} - \tilde{\rho}\overline{U}_{\perp x}. \end{aligned} \quad \text{(B3)}$$

Note that the underlined term in the continuity equation is similar to the underlined term in the budget equation. Importantly, there is a factor of $\overline{U}_\perp$ that already exists in the continuity equation (and in all the conservation equations). We cannot divide out that term, as the resulting expression would become undefined in regions of the flow where $\overline{U}_\perp = 0$ (e.g. the edges of the reversed flow region and at the wall). This motivated the modified N-factor definition.

The continuity equation is multiplied by $\tilde{\rho}^*$ and the corresponding Chu normalization factor $(\overline{T}/\gamma M^2\overline{\rho})$. The underlined terms in the 'budget terms' and in the conservation equation now match. All remaining terms in the conservation equation are moved to the right-hand side of the equation and substituted for the underlined term in the budget equation. This process is repeated with all of the conservation equations and results in a lengthy description of perturbation growth that may be used to identify single terms which dominate disturbance trends.

References

Amestoy, P.R., Buttari, A., L'Excellent, J.-Y. & Mary, T. 2019 Performance and scalability of the block low-rank multifrontal factorization on multicore architectures. *ACM Trans. Math. Softw.* **45**, 2:1–2:26.

Amestoy, P.R., Duff, I.S., Koster, J. & L'Excellent, J.-Y. 2001 A fully asynchronous multifrontal solver using distributed dynamic scheduling. *SIAM J. Matrix Anal. Appl.* **23** (1), 15–41.

Bippes, H. 1999 Basic experiments on transition in three-dimensional boundary layers dominated by crossflow instability. *Prog. Aerosp. Sci.* **35** (4), 363–412.

Borg, M.P., Kimmel, R.L. & Stanfield, S. 2015 Traveling crossflow instability for the HIFiRE-5 elliptic cone. *J. Spacecr. Rockets* **52** (3), 664–673.

CHEN, X., DONG, S., TU, G., YUAN, X. & CHEN, J. 2022*a* Boundary layer transition and linear modal instabilities of hypersonic flow over a lifting body. *J. Fluid Mech.* **938**, 1–52.

CHEN, X., XI, Y., REN, J. & FU, S. 2022*b* Cross-flow vortices and their secondary instabilities in hypersonic and high-enthalpy boundary layers. *J. Fluid Mech.* **947**, A25.

CRAIG, S.A. & SARIC, W.S. 2016 Crossflow instability in a hypersonic boundary layer. *J. Fluid Mech.* **808**, 224–244.

EDELMAN, J.B. & SCHNEIDER, S.P. 2018 Secondary instabilities of hypersonic stationary crossflow waves. *AIAA J.* **56** (1), 182–192.

EPPINK, J.L. 2020 Mechanisms of stationary cross-flow instability growth and breakdown induced by forward-facing steps. *J. Fluid Mech.* **897**, A15.

FEDOROV, A.V. & KHOKHLOV, A.P. 2002 Receptivity of hypersonic boundary layer to wall disturbances. *Theor. Comput. Fluid Dyn.* **15** (4), 231–254.

GUO, Y., MALIK, M. & CHANG, C.-L. 1997 A solution adaptive approach for computation of linear waves. In *13th Computational Fluid Dynamics Conference*. AIAA-97-2072, pp. 1111–1121. AIAA.

HANIFI, A., SCHMID, P.J. & HENNINGSON, D.S. 1996 Transient growth in compressible boundary layer flow. *Phys. Fluids* **8** (3), 826–837.

HAYNES, T.S. & REED, H.L. 2000 Simulation of swept-wing vortices using nonlinear parabolized stability equations. *J. Fluid Mech.* **405**, 325–349.

HOSSEINVERDI, S. & FASEL, H.F. 2016 Direct numerical simulations of laminar-to-turbulent transition in laminar separation bubbles in three-dimensional boundary-layer. In *46th AIAA Fluid Dynamics Conference*. AIAA-2016-3793, pp. 1–27. AIAA.

JACKSON, C.M. JR., CORLETT, W.A. & MONTA, W.J. 1981 Description and calibration of the Langley unitary plan wind tunnel. *NASA Tech. Rep.* TP-1905. NASA Langley Research Center.

JIANG, L., SHAN, H., LIU, C. & VISBAL, M.R. 1999 Non-reflecting boundary conditions for DNS in curvilinear coordinates. In *Recent Advances in DNS and LES*, pp. 219–233. Springer.

JULIANO, T.J., BORG, M.P. & SCHNEIDER, S.P. 2015 Quiet tunnel measurements of HIFiRE-5 boundary-layer transition. *AIAA J.* **53** (4), 832–846.

KNUTSON, A., GS, S. & CANDLER, G.V. 2018 Direct numerical simulation of Mach 6 flow over a cone with a highly swept fin. In *2018 AIAA Aerospace Sciences Meeting*. AIAA-2018-0379, pp. 1–14. AIAA.

KOCH, W., BERTOLOTTI, F.P., STOLTE, A. & HEIN, S. 2000 Nonlinear equilibrium solutions in a three-dimensional boundary layer and their secondary instability. *J. Fluid Mech.* **406**, 131–174.

KOHAMA, Y., SARIC, W.S. & HOOS, J.A. 1991 A high-frequency, secondary instability of crossflow vortices that leads to transition. In *Proceedings of the Conference, Boundary Layer Transition and Control, University of Cambridge, United Kingdom, April 8–12, 1991 (A93-17251 04-34)*. Royal Aeronautical Society.

LI, F., CHOUDHARI, M., PAREDES, P. & DUAN, L. 2016 High-frequency instabilities of stationary crossflow vortices in a hypersonic boundary layer. *Phys. Rev. Fluids* **1** (5), 1–32.

LIU, Z. 2022 Cross-flow linear instability in compressible boundary layers over a flat plate. *Phys. Fluids* **34** (9), 094110.

MACK, L.M. 1984 Boundary-layer linear stability theory. *Tech. Rep.* 709. AGARD.

MALIK, M., LIN, R.-S. & SENGUPTA, R. 1999 Computation of hypersonic boundary-layer response to external disturbances. In *37th Aerospace Sciences Meeting and Exhibit*. AIAA-99-0411, pp. 1–16. AIAA.

MALIK, M.R., LI, F. & CHANG, C.-L. 1994 Crossflow disturbances in three-dimensional boundary layers: nonlinear development, wave interaction and secondary instability. *J. Fluid Mech.* **268**, 1–36.

MEITZ, H.L. & FASEL, H.F. 2000 A compact-difference scheme for the Navier–Stokes equations in vorticity–velocity formulation. *J. Comput. Phys.* **157** (1), 371–403.

MIDDLEBROOKS, J.B., FARNAN, E., JULIANO, T.J., MATLIS, E.H., CORKE, T.C., PECK, M.M., MULLEN, D., REED, H.L. & SEMPER, M. 2022 Cross-flow instability experiments on a swept fin-cone with variable nose bluntness in Mach 6 flow. In *AIAA Scitech 2022 Forum*. AIAA-2022-0598, pp. 1–30. AIAA.

MIDDLEBROOKS, J.B., FARNAN, E., MATLIS, E.H., CORKE, T.C., MULLEN, C.D., PECK, M.M. & REED, H.L. 2021 Design of a hypersonic boundary layer transition control experiment utilizing a swept fin cone geometry in Mach 6 flow. In *AIAA Scitech 2021 Forum*. AIAA-2021-1205, pp. 1–19. AIAA.

MOYES, A.J., PAREDES, P., KOCIAN, T.S. & REED, H.L. 2017 Secondary instability analysis of crossflow on a hypersonic yawed straight circular cone. *J. Fluid Mech.* **812**, 370–397.

MULLEN, C.D., TURBEVILLE, F.D., REED, H.L. & SCHNEIDER, S.P. 2019 Computational and experimental boundary-layer stability analysis on a hypersonic finned cone. In *AIAA Scitech 2019 Forum*. AIAA-2019-1381, pp. 1–18. AIAA.

NIESSEN, S.E.M., GROOT, K.J., HICKEL, S. & TERRAPON, V.E. 2023 Convective instabilities in a laminar shock-wave/boundary-layer interaction. *Phys. Fluids* **35** (2), 024101.

ÖZGEN, S. & KIRCALI, S.A. 2008 Linear stability analysis in compressible, flat-plate boundary-layers. *Theor. Comput. Fluid Dyn.* **22**, 1–20.

PAREDES, P., GOSSE, R., THEOFILIS, V. & KIMMEL, R. 2016 Linear modal instabilities of hypersonic flow over an elliptic cone. *J. Fluid Mech.* **804**, 442–466.

PATEL, J.M., GROOT, K.J., SAIYASAK, C., CODER, J.G., STEFANSKI, D.L. & REED, H.L. 2022 Energy-budget analysis of the crossflow instability on a hypersonic yawed cone. In *AIAA Aviation 2022 Forum*. AIAA-2022-3777, pp. 1–16. AIAA.

PECK, M.M., GROOT, K.J. & REED, H.L. 2022*a* Boundary-layer instability on a highly swept fin on a hypersonic cone. In *AIAA Aviation 2022 Forum*. AIAA-2022-3555, pp. 1–15. AIAA.

PECK, M.M., MULLEN, D., REED, H.L., TURBEVILLE, F.D. & SCHNEIDER, S.P. 2022*b* Heat flux on a hypersonic cone with a highly swept fin. *J. Spacecr. Rockets* **59** (6), 2094–2113.

RIUS-VIDALES, A.F. & KOTSONIS, M. 2021 Impact of a forward-facing step on the development of crossflow instability. *J. Fluid Mech.* **924**, 1–35.

SARIC, W.S., REED, H.L. & WHITE, E.B. 2003 Stability and transition of three-dimensional boundary layers. *Annu. Rev. Fluid Mech.* **35** (1), 413–440.

THOMPSON, K.W. 1987 Time dependent boundary conditions for hyperbolic systems. *J. Comput. Phys.* **68** (1), 1–24.

TURBEVILLE, F.D. 2021 Measurements of transition near the corner formed by a highly-swept fin and a cone at Mach 6. PhD thesis, Purdue University.

VALLABH, B. & SKEWS, B.W. 2017 Investigation of nozzle contours in the CSIR supersonic wind tunnel. *R&D J.* **33**, 32–41.

WASSERMANN, P. & KLOKER, M. 2005 Transition mechanisms in a three-dimensional boundary-layer flow with pressure-gradient changeover. *J. Fluid Mech.* **530**, 265–293.

WHITE, E.B. & SARIC, W.S. 2005 Secondary instability of crossflow vortices. *J. Fluid Mech.* **525**, 275–308.

WRIGHT, M.J., CANDLER, G.V. & BOSE, D. 1998 Data-parallel line relaxation method for the Navier–Stokes equations. *AIAA J.* **36** (9), 1603–1609.

XU, G., CHEN, J., LIU, G., DONG, S. & FU, S. 2019 The secondary instabilities of stationary cross-flow vortices in a Mach 6 swept wing flow. *J. Fluid Mech.* **873**, 914–941.